

Cosmological implications from the full shape of the large-scale power spectrum of the SDSS DR7 luminous red galaxies

Francesco Montesano^{1,2*}, Ariel G. Sánchez² and Stefanie Phleps²

¹*Universitätssternwarte München, Scheinerstrasse 1, 81679 München, Germany*

²*Max-Planck-Institut für Extraterrestrische Physik, Giessenbachstrasse, 85748 Garching, Germany*

Accepted xxx. Received xxx; in original form xxx

ABSTRACT

We obtain cosmological constraints from a measurement of the spherically averaged power spectrum of the distribution of about 90000 luminous red galaxies (LRGs) across 7646 deg² in the Northern Galactic Cap from the seventh data release of the Sloan Digital Sky Survey. The errors and mode correlations are estimated thanks to the 160 LasDamas mock catalogues, created in order to simulate the same galaxies and to have the same selection as the data. We apply a model, that can accurately describe the full shape of the power spectrum with the use of a small number of free parameters. Using the LRG power spectrum, in combination with the latest measurement of the temperature and polarisation anisotropy in the cosmic microwave background (CMB), the luminosity-distance relation from the largest available type 1a supernovae (SNIa) dataset and a precise determination of the local Hubble parameter, we obtain cosmological constraints for five different parameter spaces. When all the four experiments are combined, the flat Λ CDM model is characterised by $\Omega_M = 0.259^{+0.016}_{-0.015}$, $\Omega_b = 0.045 \pm 0.001$, $n_s = 0.963 \pm 0.011$, $\sigma_8 = 0.802 \pm 0.021$ and $H_0 = 71.2 \pm 1.4 \text{ km s}^{-1} \text{ Mpc}^{-1}$. When we consider curvature as a free parameter, we do not detect deviations from flatness: $\Omega_k = (1.6 \pm 5.4) \times 10^{-3}$, when only CMB and the LRG power spectrum are used; the inclusion of the other two experiments do not improve substantially this result. We also test for possible deviations from the cosmological constant paradigm. Considering the dark energy equation of state parameter w_{DE} as time independent, we measure $w_{DE} = -1.025^{+0.066}_{-0.065}$, if the geometry is assumed to be flat, $w_{DE} = -0.981^{+0.083}_{-0.084}$ otherwise. When describing w_{DE} through a simple linear function of the scale factor, our results do not evidence any time evolution. In the next few years new experiments will allow to measure the clustering of galaxies with a precision much higher than achievable today. Models like the one used here will be a valuable tool in order to achieve the full potentials of the observations and obtain unbiased constraints on the cosmological parameters.

Key words: large-scale structure of Universe – cosmology: theory – cosmology: observations – cosmological parameters

1 INTRODUCTION

The last decade was characterised by a dramatic change in our vision of the Universe and by an impressive increase in size and quality of available datasets. At the end of the twentieth century, the analysis of the luminosity-distance relation in the Type 1a supernovae (SNIa) showed that the

Universe is undergoing a phase of accelerated expansion driven by a new exotic component, dubbed dark energy, whose energy density is about 70% of the total (Riess et al. 1998; Perlmutter et al. 1999). This has been then confirmed by other observations, such as the cosmic microwave background (CMB, e.g., Hinshaw et al. 2003; Spergel et al. 2003, 2007; Komatsu et al. 2009, 2011), the large scale structure of the Universe (LSS; e.g. Efstathiou et al. 2002; Percival et al. 2002; Tegmark et al. 2004; Sánchez et al. 2006, 2009;

*E-mail: montefra@mpe.mpg.de

Percival et al. 2010; Reid et al. 2010; Blake et al. 2011) and the number density of galaxy clusters as function of their mass (e.g. Vikhlinin et al 2009). Different combinations of these probes have been used in the past years to constrain the dark energy equation of state parameter w_{DE} with about a 5-10% error. The analysis presented here aims at constraining cosmological parameters and shed light on the nature of dark energy.

Many present day and future galaxy redshift surveys, like the Baryonic Oscillation Spectroscopic Survey (BOSS, Schlegel, White & Eisenstein 2009; Eisenstein et al. 2011), the Panoramic Survey Telescope & Rapid Response System (Pan-STARRS, Kaiser et al. 2002), the Dark Energy Survey (DES, Abbott et al. 2005), the Hobby Eberly Telescope Dark Energy Experiment (HETDEX, Hill et al 2004) and the space based Euclid mission (Laureijs 2009), are designed to constrain the properties of dark energy, usually parametrised by its density, the present day value of w_{DE} and its possible time evolution, with unprecedented precision. This will help to reduce the number of possible models of dark energy that has been proposed in the last decade, that are either based on a time varying field (for a review see, e.g., Peebles & Ratra 2003), or on modifications of the equation of general relativity (modified gravity, for a review see, e.g., Tsujikawa 2010).

In this work we concentrate on the distribution of galaxies on large scales as a means to constrain the history and composition of the Universe, analysing it statistically through the power spectrum, the Fourier transform of the two point correlation function. The shape of the galaxy power spectrum and correlation function contains information about the composition of the Universe and the non-linear evolution of clustering, bias (e.g. McDonald 2006; Matsubara 2008b; Jeong & Komatsu 2009) and redshift space distortions (e.g. Scoccimarro 2004; Cabré & Gaztañaga 2009a,b; Jennings, Baugh & Pascoli 2011; Reid & White 2011). Biasing is due to the fact that the objects that we observe do not trace perfectly the underlying dark matter distribution and redshift space distortions are introduced when inferring the distance of a galaxy from the measured redshift, which is a sum of a cosmological component and a Doppler shift due to the peculiar motion of the emitter. The two-point statistics contain also a feature, called baryonic acoustic oscillations (BAO), that has been advocated as a powerful tool to probe the curvature of the Universe and that has been intensively studied over the past years. BAOs are the relic signature in the matter distribution of the acoustic oscillations in the baryon-photon plasma in the hot young Universe. The BAOs show up in the correlation function as a quasi gaussian bump at scales $r \approx 100 - 110 h^{-1} \text{Mpc}$ (Matsubara 2004) and as a sequence of damped quasi-acoustic oscillations at wave-numbers $0.01 h \text{Mpc}^{-1} < k < 0.4 h \text{Mpc}^{-1}$ in the power spectrum (Sugiyama 1995; Eisenstein & Hu 1998, 1999). BAOs in the CMB were predicted by Peebles & Yu (1970) and Sunyaev & Zeldovich (1970) and first detected in the galaxy distribution by Cole et al. (2005) and Eisenstein et al. (2005). The BAO scale, as measured from the CMB, depends only on the plasma physics prior to recombination, which allows in principle to use it as a standard ruler. Non linear evolution damps and shifts by few percent the acoustic peaks

(Crocce & Scoccimarro 2008; Sánchez, Baugh & Angulo 2008; Smith, Scoccimarro & Sheth 2008). The full shape of the power spectrum and of the correlation function, as well as the BAOs alone, have been used, alone and in combination with other independent datasets, to constrain cosmological parameters (e.g., Percival et al. 2007; Sánchez & Cole 2008; Cabré & Gaztañaga 2009a; Gaztañaga, Cabré & Hui 2009; Sánchez et al. 2009; Kazin et al. 2010; Percival et al. 2010; Reid et al. 2010; Blake et al. 2011; Tinker et al. 2011).

In order to obtain unbiased constraints from the information encoded in the large scale structure of the Universe, non linear distortions, bias and redshift space distortions need to be accounted for. Perturbation theory (PT, see Bernardeau et al. 2002, for a review) can successfully model the shape of the power spectrum and of the correlation function at redshifts larger than $z = 1$ or at large scales when including at least third order terms in the density fluctuations (Jeong & Komatsu 2006, 2009). In the past few years many groups have proposed different improvements over perturbation theory (e.g., Crocce & Scoccimarro 2006a,b; McDonald 2007; Matarrese & Pietroni 2007; Bernardeau, Crocce & Scoccimarro 2008; Matarrese & Pietroni 2008; Matsubara 2008a,b; Pietroni 2008; Taruya & Hiramatsu 2008; Smith, Hernández-Monteagudo & Seljak 2009; Taruya et al. 2009; Elia et al. 2010). While some of this approaches, like for instance Matsubara (2008b) and Taruya, Nishimichi & Saito (2010), can account for bias and redshift space distortions, most of them describe only the clustering of dark matter in real space. For this reason phenomenological approaches based on a given flavour of PT have been put forward in order to model the dark matter halo and galaxy distributions in real and in redshift space (e.g., McDonald 2006; Crocce & Scoccimarro 2008; Sánchez, Baugh & Angulo 2008; Jeong & Komatsu 2009; Montesano, Sánchez & Phleps 2010, the latter will be thereafter referred to as M10). The model proposed by M10 is inspired by renormalised perturbation theory (RPT Crocce & Scoccimarro 2006a,b) and can describe the full shape of the mildly non-linear the dark matter and halo-power spectrum from numerical N-body simulation and allows to obtain unbiased constraints on the dark energy equation of state parameter.

In this analysis we apply the model developed and tested in M10 to the power spectrum measured from the luminous red galaxies (LRGs), released publicly in the seventh data release of the Sloan Digital Sky Survey (SDSS DR7). Combining this measurement with the latest results from CMB, SNIa and the precise determination of the local Hubble constant, H_0 , we obtain cosmological constraints for five different parameter spaces. The LRG sample and the mock catalogues used to estimate the covariance matrix of the data are presented in Section 2. The power spectra and covariance matrix computed from the real and mock datasets are shown in Section 3. The CMB and SNIa datasets and the H_0 measurement are described in Section 4. Section 5.1 gives a short description of the model that we apply to the LRG power spectrum. In Sections 5.2 and 5.3 we illustrate the parameter spaces that we explore in our analysis and the technique used to perform the fits. In Section 5.4 we test our model against the mean power spectrum of the mock catalogues and of the LRG, in order to determine whether it can

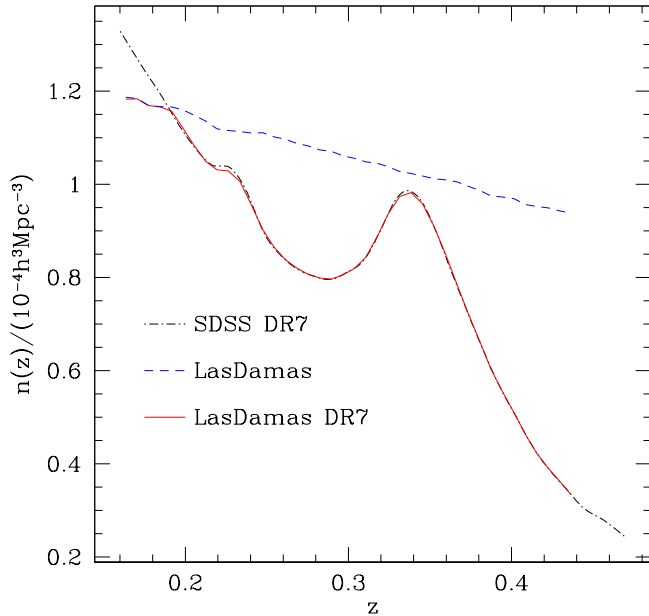


Figure 1. Spline fit to the redshift distribution of the LRGs (dot-dashed line) and the original and modified $n(z)$ of the mock catalogues (dashed and solid lines, respectively)

describe accurately the full shape of the two-point statistic when a complex geometry is used. Our main results, the cosmological constraints for the five parameter spaces, are discussed in Section 6 and then compared with some of the most recent works on the topic in Section 7. Finally we summarise our results and draw our conclusions in Section 8.

2 THE GALAXY SAMPLE AND THE MOCK CATALOGUES.

In this section we describe the galaxy sample (Section 2.1) and the mock catalogues (Section 2.2) that we use in this work.

2.1 The luminous red galaxy sample from the 7th data release of SDSS

Data release 7 (DR7, Abazajian et al. 2009) is the last data release of the second phase of SDSS, known as SDSS-II. From the 929,555 galaxies, whose spectra have been measured, we use the subsample of luminous red galaxies (LRGs, Eisenstein et al. 2001) presented in Kazin et al. (2010) and publicly available¹. The catalogue contains 89,791 LRGs, in the redshift range $0.16 < z < 0.44$ ($\bar{z} = 0.314$), from the large contiguous area of 7646 deg^2 in the Northern Galactic Cap. The full survey also includes three equatorial stripes, that we do not consider. This causes a loss of less than 10% in galaxy number and volume, but the resulting geometry is simpler. Furthermore, the use of the Northern Galactic Cap only allows us to obtain a more accurate estimate of the statistical errors than for the full survey (see Section 2.2). The dot-dashed line in Figure 1 shows a smooth spline fit to

Table 1. Cosmological parameters and specifications of the LasDamas-Oriana simulations

matter density	Ω_m	0.25
cosmological constant density	Ω_Λ	0.75
baryonic density	Ω_b	0.04
Hubble parameter [$\text{km s}^{-1} \text{ Mpc}^{-1}$]	H	70
amplitude of density fluctuations	σ_8	0.8
scalar spectral index	n_s	1.0
number of particles	N_p	1280 ³
box size [$h^{-1} \text{ Mpc}$]	V	2400
particle mass [$10^{10} M_\odot$]	M_p	45.73
softening length [$h^{-1} \text{ kpc}$]	ϵ	53

the sample number density as function of redshift. Together with the LRGs catalogue, we use a random one with about fifty times more objects, designed to reproduce the geometry and completeness of the galaxy sample and to have a radial number density proportional to the dot-dashed line in Figure 1.

2.2 The mock catalogues

In order to test our analysis technique and to estimate the covariance matrix associated to the LRG power spectrum, we use the *LasDamas* mock catalogues (McBride et al., in prep.). The mocks have been constructed from a suite of 40 large dark matter N-body simulations, dubbed *Oriana*, that reproduce a part of a universe characterised by a geometrically flat cosmology dominated by a cosmological constant and cold dark matter (ΛCDM). The cosmological parameters and specifications of the simulations are listed in Table 1. From each simulation a halo catalogue is extracted using a Friend-of-Friend algorithm (FoF, Davis et al. 1985) with linking length 0.2 times the mean inter-particle separation. In order to match the LRG clustering signal, the haloes have then been populated with mock galaxies using a halo occupation distribution (HOD, Berlind & Weinberg 2002) within the halo model approach (HM, see Cooray & Sheth 2002, for a review). The HOD parameters have been chosen in order to reproduce the galaxy number density and the projected correlation function of the observed SDSS DR7 samples. From each simulation two (four) mock catalogues of the full SDSS DR7 volume (Northern Galactic Cap only) have been extracted. These mock catalogues, together with the mocks from two smaller companions of Oriana and the corresponding randoms, are publicly available².

In this work we use the 160 mock catalogues of the LRGs in the Northern Galactic Cap region. We modify the mocks and the corresponding random catalogue, which have the radial number density shown by the dashed line in Figure 1, in order to reproduce the one of the LRG: the resulting $n(z)$ is indicated by the solid line. The mock catalogues contain on average 91137 galaxies.

¹ <http://cosmo.nyu.edu/~eak306/SDSS-LRG.html>

² <http://lss.phy.vanderbilt.edu/lasdamas>

3 THE POWER SPECTRA

From the dataset and the mock catalogues just described we compute the power spectra and the covariance matrix that are used in the rest of the analysis. They are presented in this section.

3.1 The LRG power spectrum

To compute the power spectrum and the window function we need to convert the angular positions and redshifts of the galaxies and of the random points into comoving coordinates. This is done first inferring radial distances from the measured redshifts and then converting the spherical coordinates into cartesian ones. To do the first step we assume as fiducial the cosmology of the LasDamas simulations, shown in Table 1.

We compute the power spectrum, as well as the survey window function, using the estimator introduced by Feldman, Kaiser & Peacock (1994, thereafter FKP). Percival, Verde & Peacock (2004, thereafter PVP) proposed a modification of the FKP approach to take into account the relative biases between populations with different luminosities. In Appendix B1 we show that, thanks to the fact that the LRG sample is almost volume limited and composed by a relatively homogeneous class of galaxies, the shape of the power spectra recovered with the two methods are in excellent agreement at linear and mildly non-linear scales. In Appendix A we summarise the most important equations of both estimators.

At first we correct the galaxy catalogue for the loss of objects due to fibre collisions (Zehavi et al. 2002; Masjedi 2006). The SDSS spectrographs are fed by optical fibres plugged on plates, which forces the fibres to be separated by at least $55''$. It is then impossible, in a single exposure, to obtain spectra of galaxies nearer than this angular distance. The problem is partially alleviated by multiple exposures, but it is not possible to observe all the objects in crowded regions. Assuming that in a given region of the n galaxies that satisfy the selection criteria we can measure only $m \leq n$ redshifts due to fibre collision and assuming that the missed galaxies have the same redshift distribution of the observed ones, we assign to the latter a weight $w_i = n/m$. This ensures that the sum of the weights in a given region of the sky is equal to the number of selected galaxies n . Secondly to each LRG and random object at position \mathbf{x} , where the number density is $n(\mathbf{x})$, we associate a weight $w(\mathbf{x}) = (1 + p_w n(\mathbf{x}))^{-1}$, with $p_w = 40000 h^{-3} \text{Mpc}^3$. This value has been chosen in order to minimise the variance of the measured power spectrum in the range $0.02 h \text{Mpc}^{-1} \leq k \leq 0.2 h \text{Mpc}^{-1}$. In Appendix B1 we show the results of the tests to analyse the impact of different choices of p_w and corrections, namely fibre collision and completeness, on the recovered power spectrum.

To compute the power spectrum we assign the LRGs and the random objects, weighted as described before, to a cubic grid with $N = 1024^3$ cells and side $L = 2200 h^{-1} \text{Mpc}$ using triangular shaped cloud (TSC) as mass assignment scheme (MAS). For each cell, we compute the $F(\mathbf{x})$ field of equation (A1a). We then perform the fast Fourier transform

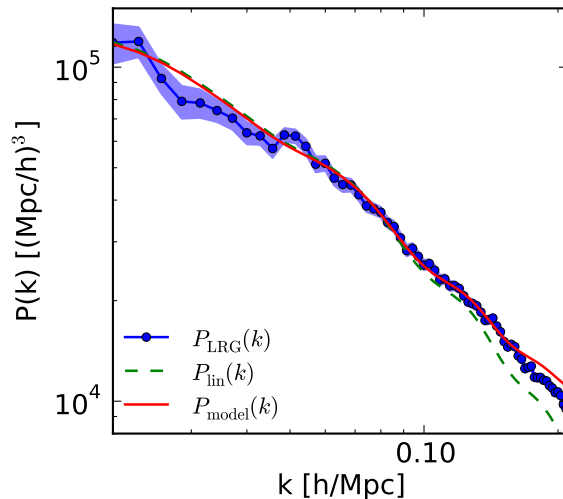


Figure 2. LRGs power spectrum (blue dots connected with solid line) and corresponding $1\text{-}\sigma$ error bars from the mock catalogues (shaded area). The green dashed and the red solid lines show, respectively, the linear and model power spectra computed using the mean value of the cosmological parameters of the ΛCDM cosmology show in the last column of Table 3.

(FFT) using the publicly available software FFTW³ (Fastest Fourier Transform in the West, Frigo & Johnson 2005). We correct each Fourier mode by dividing it by $\sum_{\mathbf{n}} |W(\mathbf{k} - 2k_N \mathbf{n})|^2$, where $W(\mathbf{k})$ is the Fourier transform of TSC, $k_N = \pi(N^{1/3}/L)$ is the Nyquist wavenumber and \mathbf{n} is a 3D integer vector. Finally we spherically average the Fourier modes and subtract the shot noise (equation A5a).

The window function is evaluated similarly. We assign the objects of the random catalogue to four cubic grids with $N = 1024^3$ cells and sides $L = 2200, 4400, 8800$ and $17600 h^{-1} \text{Mpc}$ and compute the field $\tilde{G}(\mathbf{x})$ of equation (A6a). We use the four grids with different dimensions in order to be able to compute the window function up to very large scales. For each box, we perform the FFT, correct the Fourier modes, spherical average and subtract the shot noise (equation A7a). For each window function $G^2(k)$, we discard all the modes with wave-number $k > 0.65 k_N$ and, when two or more window functions overlap, we consider only the one computed in the larger volume. This choice is motivated by the fact that, for a given band in wavenumber, the larger volume window function has been computed averaging over a larger number of modes than the ones from smaller volumes. Finally we merge the four window functions in order to obtain a single curve.

According to equation (A4), the observed power spectrum $P_o(k)$ just described is a convolution of the “true” power spectrum $P_t(k)$ with the window function. This convolution is computationally time consuming, in particular when it has to be performed repetitively. Therefore we transform this convolution into a matrix multiplication:

$$P_o(k_i) = \sum_n W(k_i, k_j) P_t(k_j) - C G^2(k_i). \quad (1)$$

³ <http://www.fftw.org/>

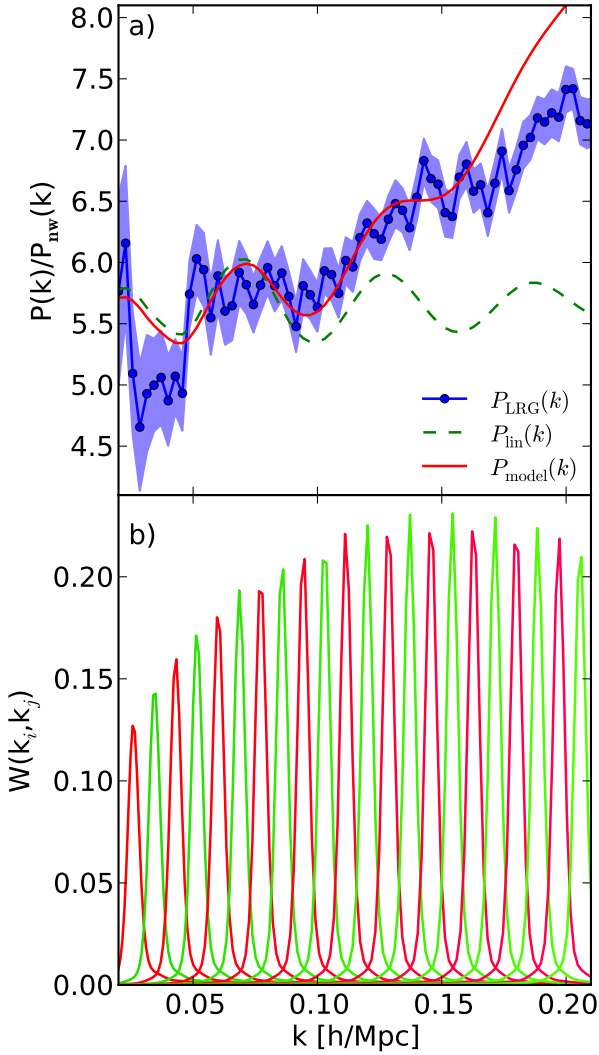


Figure 3. Panel a): power spectra of Figure 2 divided by a linear power spectrum without BAOs (Eisenstein & Hu 1998). Panel b): rows of the window matrix corresponding to the k -bands of the measured LRG power spectrum. For clarity only one every third row is shown.

$W(k_i, k_j) = a_j k_j^2 \int_{-1}^1 d\cos(\theta) G^2(|\mathbf{k}_i - \mathbf{k}_j|)$ is the window matrix normalised such that $\sum_j W(k_i, k_j) = 1 \forall i$. The coefficients a_j corresponding to the wavenumber k_j are derived using the Gauss-Legendre decomposition. The second term in the right hand side arises from the integral constraint (Percival et al. 2007) where C is a constant determined by requiring that $P_0(0) = 0$.

The LRG power spectrum is shown in Figure 2 with blue dots connected by a solid line. We also show the linear (green dashed line) and the model (red solid line) power spectra computed from the best fit parameters obtained assuming a flat Λ CDM cosmology (see section 6.1 for more details). Both of the power spectra have been convolved with the window function as in equation (1) and their amplitude has been boosted in order to match the observed one. The blue shaded area represent the variance from the mock catalogues. Panel a) of Figure 3 shows the same quantities, with

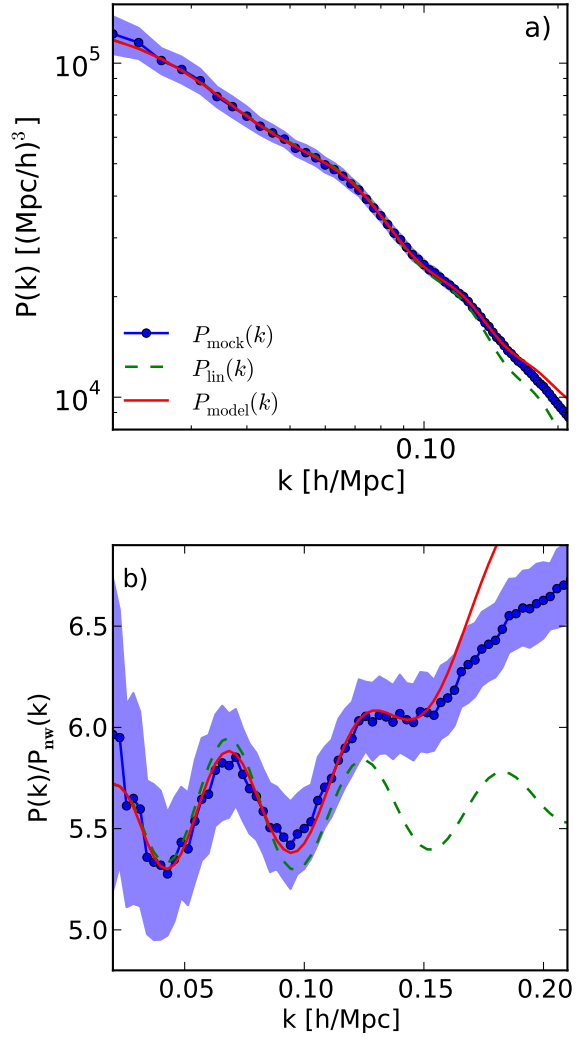


Figure 4. Panel a): mean power spectrum (blue dots connected by solid line) with $1\text{-}\sigma$ variance (blue shaded area) from the mock catalogues. The linear and model power spectra, convolved with the window function, are shown with green dashed and red solid lines, respectively. Panel b): same power spectra divided by a linear power spectrum without BAOs (Eisenstein & Hu 1998).

the same colour and line coding, but divided by a smooth linear power spectrum without BAOs (Eisenstein & Hu 1998).

Panel b) of Figure 3 shows one every third row of the window matrix $W(k_i, k_j)$. Because of the relatively simple and uniform geometry of the sample used, the window function has its maximum at $k = 0 \text{ h Mpc}^{-1}$ and decreases very steeply. This translates into the very sharp peaks at $k_j \sim k_i$ in the window matrix rows, as shown in the figure.

3.2 The mock power spectra and covariance matrix

We compute the power spectra from the 160 realisations and the window function as we do for the LRG sample in the previous section. We then compute the mean $\bar{P}(k)$, the standard deviation and the covariance matrix \mathbf{C} , whose ele-

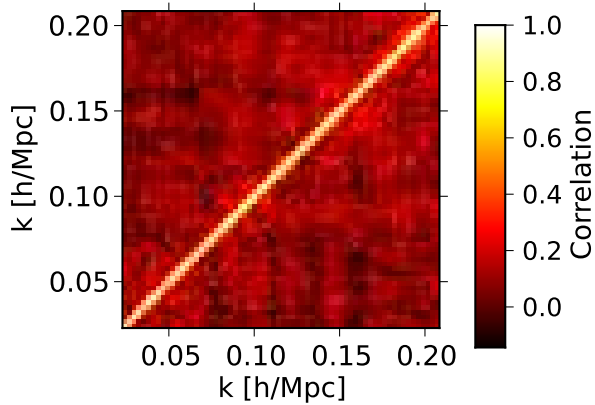


Figure 5. Correlation matrix computed from the LasDamas mock catalogues.

ments are defined by:

$$C_{mn} = \frac{1}{N_{\text{real}} - 1} \sum_{l=1}^{N_{\text{real}}} (P_l(k_m) - \bar{P}(k_m))(P_l(k_n) - \bar{P}(k_n)), \quad (2)$$

where $P_l(k_m)$ corresponds to the measurement of the power spectrum at the m -th k -bin in the l -th realisation.

Panel a) of Figure 4 shows the mean power spectrum and its variance (blue dots with solid line and shaded area) obtained from the mock catalogues. The green dashed and the red solid lines show the linear and the best fit model power spectra (see Section 5.4.1 for more details) convolved with the window function of the mocks and rescaled by the bias. Panel b) of Figure 4 shows the same power spectra of panel a) divided by a power spectrum without oscillations $P_{\text{nw}}(k)$.

The correlation matrix of the mock catalogues, defined as $C_{mn}/\sqrt{C_{mm}C_{nn}}$, is shown in Figure 5. The mode correlation caused by the convolution with the window function is visible in particular near the diagonal. Non linear mode coupling is present at small scales and its strength increases with increasing k . Although the correlation becomes important for $k > 0.2 h \text{ Mpc}^{-1}$, it is not negligible already at $k \approx 0.1 h \text{ Mpc}^{-1}$. Recently Samushia, Percival & Raccanelli (2011) showed that different methods of constructing the random catalogues can affect the estimated covariance matrix.

The version of the mocks available when writing this article does not contain information about the luminosity of the galaxies, completeness and fibre collision. We cannot therefore test the impact of different estimators and corrections on the errors. However we analyse the impact of different p_w on the power spectra and errors as measured from the mocks: the results are reported in Appendix B2.

4 ADDITIONAL EXPERIMENTS

Later in this article we use the measurement of the LRG power spectrum described in the previous section to constrain cosmological parameters. In order to obtain tight constraints it is not possible to use this measurements alone, since some parameters have a weak dependence on the shape

of the power spectrum and others present strong degeneracies. Using the information coming from independent experiments, like the cosmic microwave background (Section 4.1) and the type 1a supernovae (Section 4.2), or prior knowledge of some of the parameters, like the local Hubble parameter (Section 4.3), it is possible to greatly improve the accuracy of the analysis.

4.1 Cosmic microwave background

Accurate measurements of the CMB temperature and polarisation anisotropies provide a powerful tool to constrain cosmological parameters. In this work we use the observations from five different instruments.

The Wilkinson Microwave Anisotropy Probe (WMAP) satellite produced full sky maps of the CMB with a resolution of 0.2° . We make use of the temperature angular power spectrum in the multipole range $2 \leq l \leq 1000$ and the temperature-E polarisation cross power spectrum in the range $2 \leq l \leq 450$ from the 7th year data release (WMAP7, Jarosik et al. 2010; Komatsu et al. 2011; Larson et al. 2011).

We also use measurements of higher multipoles from other four experiments which observe the CMB temperature anisotropy on small patches of the sky with a much higher resolution. In order to avoid complex correlations, we use these experiments only for multipoles that do not overlap with the WMAP measurements. We use the measurements of the temperature angular power spectrum i) in 14 bandpowers in the range $910 \leq l \leq 1850$ from the Arcminute Cosmology Bolometer Array (ACBAR, Kuo et al. 2007; Reichardt et al. 2009), ii) in 6 bandpowers in the range $855 \leq l \leq 1700$ from the Cosmic Background Imager (CBI, for latest results see Sievers et al. 2009), iii) in 7 bandpowers in the range $925 \leq l \leq 1400$ from the 2003 flight of the Balloon Observations Of Millimetric Extragalactic Radiation and Geophysics (BOOMERanG Jones et al. 2006; MacTavish et al. 2006; Montroy et al. 2006; Piacentini et al. 2006) and iv) in 11 bandpowers in the range $974 < l < 1864$ from the final data release of QUEST at DASI (QUAD, for latest results see Brown et al. 2009). We also use E and B polarisation (EE and BB) and the cross temperature-E polarisation (TE) angular power spectra measurements from the latter three experiment. i) CBI: EE in 7 bandpowers in the range $860 \leq l \leq 1800$, BB in 5 bandpowers in the range $0 \leq l \leq 5000$ and TE in 8 bandpowers in the range $860 \leq l \leq 1800$; ii) BOOMERanG: EE and BB in 3 bandpowers in the range $600 < l < 1000$ and TE in 6 bandpowers in the range $450 \leq l \leq 950$; iii) QUAD: EE, BB and TE in 17 bandpowers in the range $488 < l < 1864$.

4.2 Type 1a supernovae

Type 1a supernovae (SNIa) provided the first evidences of an accelerating Universe and the need of a new exotic component, called dark energy, to explain it (Riess et al. 1998; Perlmutter et al. 1999). From the light curve, i.e. the luminosity variation as function of time, of a SNIa it is possible to measure the absolute luminosity, from which the distance to each object is inferred, probing in this way the distance-redshift relation. The first step is performed

thanks to models which encode intrinsic variations due to the physics of the SNIa, the effects from galactic and intergalactic medium and selection effects in different ways. Because of this, models produce different results, which impact the accuracy at which cosmological parameters can be measured and can introduce systematic effects (e.g. Hicken et al. 2009; Kessler et al. 2009).

SNIa data have been collected by many surveys designed according to different strategies and carried out using a large variety of telescopes. Each of them observes a relatively small number of events, typically less than a hundred. In order to increase the number of objects, recently collections of SNIa from different surveys have been created. In this work we use one of such samples, the Union2 (Amanullah et al. 2010). It consists of 557 SN drawn from 17 datasets in the redshift range $0.015 \leq z \leq 1.4$ and is the largest available supernovae sample to date. It extends and improves the Union (Kowalski et al. 2008) and the Constitution (Hicken et al. 2009) datasets: all the light curves of the selected SNIa have been fitted with SALT2 (Guy et al. 2007) and an improved analysis of systematics is presented. Amanullah et al. (2010) showed that the inclusion of systematic errors when fitting cosmological parameters, using only SNIa or in combination with independent probes (BAO, CMB and H_0), increases the associated errors leaving the best fit value almost unchanged. In Sections 6.1 and 6.3 we will further comment on the impact of systematics and of light curve fitters.

4.3 Hubble parameter

The Supernovae and H_0 for the Equation of State Program (SHOES, Riess et al. 2009) aims at the direct measurement of the Hubble parameter at present epoch H_0 to better than 5% accuracy. The SHOES team identified 6 nearby spectroscopically typical SNIa, that have been observed before maximum luminosity, that reside in galaxies containing Cepheids and that are subjects to low reddening. Thanks to 260 Cepheids observed with the Near-Infrared Camera and Multi-Object Spectrometer (NICMOS) on the Hubble Space Telescope (HST) in the 6 host galaxies and in the “maser galaxy” NGC 4258, the authors could calibrate directly the peak luminosity of the SNIa. Combining these 6 objects with 240 SNIa at redshift $z < 0.1$, they measure the Hubble parameter to be $H_0 = 74.2 \pm 3.6 \text{ km s}^{-1} \text{ Mpc}^{-1}$. The error includes both statistical and systematic uncertainties. In this work we use this result as a prior knowledge of H_0 , under the assumption that the associated likelihood is a gaussian with the mean and standard deviation measured by the SHOES team.

Recently Moresco et al. (2010) measured, using spectral properties of early-type galaxies, the Hubble parameter to be $H_0 = 72.6 \pm 2.9 \text{ km s}^{-1} \text{ Mpc}^{-1}$ at 68% confidence level. While finishing this work, Riess et al (2011) refined their analysis obtaining $H_0 = 73.8 \pm 2.4 \text{ km s}^{-1} \text{ Mpc}^{-1}$.

5 METHODOLOGY

In this section we describe the model for the full shape of the power spectrum that we use throughout the rest of this article (Section 5.1). In Sections 5.2 and 5.3, we present the pa-

rameter spaces explored in Section 6 and the method used to extract cosmological information. Finally, we test the model against the LasDamas and the LRG power spectra (Section 5.4).

5.1 The model

M10 introduced a model for the full shape of the power spectrum inspired by renormalized perturbation theory (RPT, Crocce & Scoccimarro 2006a,b) and analogous to the one for the correlation function of Crocce & Scoccimarro (2008) and Sánchez, Baugh & Angulo (2008). In this model they parametrize the non-linear power spectrum as

$$P(k, z) = b^2 \left(e^{-(k/k_*)^2} P_L(k, z) + A_{MC} P_{1\text{loop}}(k, z) \right), \quad (3)$$

where the linear bias b , the damping scale of the BAO oscillations k_* and amplitude of the mode coupling contribution A_{MC} are free parameters. $P_L(k, z)$ is the linear power spectrum and

$$P_{1\text{loop}}(k) = \frac{1}{4\pi^3} \int d^3q |F_2(\mathbf{k} - \mathbf{q}, \mathbf{q})|^2 P_L(|\mathbf{k} - \mathbf{q}|) P_L(q) \quad (4)$$

is the lowest order term arising from the coupling of two initial modes. The exponential damping and $P_{1\text{loop}}(k)$ are the approximations of the non-linear propagator and of the mode coupling power spectrum described by RPT.

The model of equation (3) has been successfully tested in M10 against a suite of very large, median resolution N-body numerical simulations, called L-BASICC II (Angulo et al. 2008; Sánchez, Baugh & Angulo 2008). M10 computed power spectra for the dark matter distribution and several halo samples, selected according to their mass, both in real and redshift space at $z=0, 0.5$ and 1. They have shown that in all cases equation (3) describes accurately these power spectra for $k \lesssim 0.15 h \text{ Mpc}^{-1}$ and that it allows to obtain unbiased constraints on cosmological parameters.

5.2 Parameter spaces

In the description of the datasets presented in Sections 2-4, a strong assumption was implicitly made: the Universe is, at large scales, statistically homogeneous and isotropic and that density and velocity fluctuations around their mean values are small. In the following, we further assume that the fluctuations set by the initial conditions were adiabatic, gaussian and almost scale invariant and that they do not present tensor modes. The WMAP7 data, both alone and in combination with BAO, H_0 and SNIa, confirm that those assumptions are correct at the 95% confidence level (Komatsu et al. 2011; Larson et al. 2011).

Within this framework we analyse five different cosmological models, explored using five combinations of experiments: CMB, CMB+ $P_{\text{LRG}}(k)$, CMB+ $P_{\text{LRG}}(k)+H_0$, CMB+ $P_{\text{LRG}}(k)+\text{SNIa}$ and CMB+ $P_{\text{LRG}}(k)+H_0+\text{SNIa}$.

The “concordance” Λ CDM model is the simplest model able to successfully describe a large variety of cosmological datasets. It describes a geometrically flat ($\Omega_k = 0$) universe with a cosmological constant Λ , whose equation of state parameter $w_{\text{DE}} = -1$ is constant in space and time, and pressureless cold dark matter (CDM) as main components. This cosmology can be characterised by six parameters: the baryon and dark matter densities $\omega_b = \Omega_b h^2$ and

$\omega_{\text{DM}} = \Omega_{\text{DM}} h^2$, the scalar spectral index n_s and the amplitude A_s of the primordial fluctuations, the optical depth τ to the last scattering surface, assuming instantaneous reionisation, and the ratio between the horizon scale at decoupling and the angular diameter distance to the corresponding redshift Θ :

$$\theta_{\Lambda\text{CDM}} = (\omega_b, \omega_{\text{DM}}, n_s, A_s, \tau, \Theta; b, k_*, A_{\text{MC}}, A_{\text{SZ}}). \quad (5)$$

The four parameters after the semicolon are related to the modelling of the matter power spectrum (b , k_* and A_{MC} from equation 3) and of the CMB angular power spectrum (A_{SZ} , amplitude of the contribution to the CMB at large l from the Sunyaev-Zeldovich effect). These parameters are marginalised over when showing the cosmological constraints in the section 6.

If we then drop one or both assumptions on geometry and on the value of the dark energy equation of state, we obtain three cosmologies characterised by the following parameter spaces:

- variable curvature, $w_{\text{DE}} = -1$:

$$\theta_{k\Lambda\text{CDM}} = (\omega_b, \omega_{\text{DM}}, \Omega_k, n_s, A_s, \tau, \Theta; b, k_*, A_{\text{MC}}, A_{\text{SZ}}); \quad (6)$$

- zero curvature, $w_{\text{DE}} = \text{const}$:

$$\theta_{w\text{CDM}} = (\omega_b, \omega_{\text{DM}}, w_{\text{DE}}, n_s, A_s, \tau, \Theta; b, k_*, A_{\text{MC}}, A_{\text{SZ}}); \quad (7)$$

- variable curvature, $w_{\text{DE}} = \text{const}$:

$$\theta_{kw\text{CDM}} = (\omega_b, \omega_{\text{DM}}, \Omega_k, w_{\text{DE}}, n_s, A_s, \tau, \Theta; b, k_*, A_{\text{MC}}, A_{\text{SZ}}). \quad (8)$$

As last case, we consider a flat Universe in which $w_{\text{DE}}(a)$ evolves with time. We adopt the parametrisation proposed by Chevallier & Polarski (2001) and Linder (2003):

$$w_{\text{DE}}(a) = w_0 + w_a(1 - a). \quad (9)$$

Although not physically motivated, it can describe accurately a big variety of equations of state derived from scalar fields with the use of only two parameters: its value today, w_0 , and its first derivative with respect to a , w_a . The resulting parameter space is:

$$\theta_{wa\text{CDM}} = (\omega_b, \omega_{\text{DM}}, w_0, w_a, n_s, A_s, \tau, \Theta; b, k_*, A_{\text{MC}}, A_{\text{SZ}}). \quad (10)$$

Other cosmological quantities can be derived from the ones just listed. In particular we are interested in:

$$\theta_{\text{der}} = (\Omega_{\text{DE}}, \Omega_{\text{M}}, H, t_0, \sigma_8, z_{\text{re}}). \quad (11)$$

The density of dark energy, Ω_{DE} , is obtained from a combination of Ω_k , $\omega_{\text{M}} = \omega_b + \omega_{\text{DM}}$ and Θ . From there, the total matter density $\Omega_{\text{M}} = 1 - \Omega_k - \Omega_{\text{DE}}$, the Hubble parameter $h = \sqrt{\omega_{\text{M}}/\Omega_{\text{M}}}$ and the age of the universe $t_0 = \int_0^1 da/(aH(a))$ are derived. The present day *rms* of linear density fluctuation in a sphere of radius $8 h^{-1}$ Mpc, σ_8 , is computed from A_s . From τ , H , Ω_b and Ω_{DM} it is possible to estimate the redshift of reionisation z_{re} (Tegmark, Silk & Blanchard 1994).

5.3 Practical issues

To constrain the sets of cosmological and model parameters just described, we use the Markov Chain Monte Carlo technique (MCMC, Gilks, Richardson & Spiegelhalter

Table 2. Prior ranges for the primary cosmological and the model parameters

Parameter	lower limit	upper limit
$\omega_b = \Omega_b h^2$	0.005	0.1
$\omega_{\text{DM}} = \Omega_{\text{DM}} h^2$	0.01	0.99
Ω_k	-0.3	0.3
$w_{\text{DE}} (w_0)$	-2	0
w_a	-2	2
n_s	0.5	1.5
$\log(10^{10} A_s)$	2.7	4
τ	0.01	0.8
100Θ	0.5	10
k_*	0.01	0.35
A_{MC}	0	5
A_{SZ}	0	2

1996; Christensen & Meyer 2000) as implemented in the free software COSMOMC⁴ (Cosmological MonteCarlo, Lewis & Bridle 2002). The CMB and linear matter power spectra are computed with a modified version of CAMB (Code for Anisotropies in the Microwave Background, Lewis, Challinor & Lasenby 2000) that allows to consider time varying w_{DE} ⁵ (Fang, Hu & Lewis 2008). For each choice of parameter space and probes we run eight independent chains. Their execution is stopped when the Gelman & Rubin (1992) criterion $R < 1.02$ is satisfied. The MCMC requires some prior knowledge of the parameter space that is explored. We assume for all the primary parameters (equations 5-8 and 10) flat priors in the ranges listed in Table 2. The model parameter b is analytically marginalised over an infinite flat prior (equation F2 in Lewis & Bridle 2002).

All likelihoods used to compare the results from the cosmological probes described in sections 2.1, 4.1, 4.2 and 4.3 with the corresponding models are assumed to be Gaussian. In the case of the LRGs power spectrum, this is

$$\mathcal{L} \propto \exp\left(-\frac{1}{2}\chi^2(\theta)\right), \quad (12)$$

where

$$\chi^2(\theta) = (\mathbf{d} - \mathbf{t}(\theta))^T \mathbf{C}^{-1} (\mathbf{d} - \mathbf{t}(\theta)) \quad (13)$$

is the standard χ^2 , in which \mathbf{d} is an array containing the band power $P(k)$, $\mathbf{t}(\theta)$ contains the model computed for the set of parameters θ and then convolved with the window function and \mathbf{C} is the covariance matrix of the measurement presented in section 3.2.

In section 2.1 we assume a fiducial cosmology in order to convert redshifts and angles to physical coordinates. Different choices of these parameters result in modifications of the measured LRG power spectrum. The ideal case would be to recompute, for each step of the MCMC chain, the power spectrum and the window function according to the given cosmology, but this is not computationally feasible. Under the assumption that the survey covers a wide solid angle,

⁴ <http://cosmologist.info/cosmomc/>

⁵ <http://camb.info/ppf/>

it is possible to incorporate these distortions in the correlation function when computed using different cosmologies by rescaling the distance scale by the factor (Eisenstein et al. 2005):

$$\alpha = \frac{D_V^{\text{model}}(z_m)}{D_V^{\text{fid}}(z_m)}, \quad (14)$$

where the effective distance $D_V(z_m)$ to the mean redshift of the sample z_m is,

$$D_V(z) = \left[D_A^2(z) \frac{cz_m}{H(z_m)} \right]^{1/3}, \quad (15)$$

with $D_A(z_m)$ the comoving angular diameter distance. Since the power spectrum is the Fourier transform of the correlation function, this holds also for the former. Thus, at each step of the chain we multiply the wave-number of the model power by α and its amplitude by $1/\alpha^3$ in order to rescale it to the fiducial cosmology.

5.4 Testing the model

In the first part of this section we extend the analysis of M10 and fit our model against the mock catalogues in order to test whether it provides an accurate description of the measured power spectrum and unbiased constraints of the dark energy equation of state parameter also when a complex geometry is involved. We also test the stability of the cosmological parameters in the Λ CDM case as the maximum k included in the analysis varies, when CMB and the $P_{\text{LRG}}(k)$ are combined.

5.4.1 Mock catalogues

In this section we follow M10 and assume all the parameters fixed, except for w_{DE} . Under this assumption, equation (14) links univocally variations of the dark energy equation of state to stretches α of the model power spectrum. Therefore we consider the latter as a free parameter (Huff et al. 2007).

Using a MCMC approach, we explore the parameter space defined by $\theta = (k_*, b, A_{\text{MC}}, \alpha)$. We chose priors with a constant probability within the following ranges:

- $0 \, h \, \text{Mpc}^{-1} < k_* < 0.35 \, h \, \text{Mpc}^{-1}$,
- $0 \leq A_{\text{MC}} < 10$,
- $0.5 \leq \alpha < 1.5$.

The bias b is marginalised analytically over an infinite flat prior as described in section 5.3.

Figure 6 shows the one-dimensional marginalised constraints on the parameters k_* , A_{MC} and α varying the maximum value of the wave number k_{max} of the measured power spectrum used to perform the fit; we keep the minimum k fixed to $0.02 \, h \, \text{Mpc}^{-1}$. The blue circles connected by solid lines and the shaded areas correspond to the mean and the standard deviation of these parameters. For every k_{max} the model is evaluated for $k \leq 0.2 \, h \, \text{Mpc}^{-1}$ and then convolved with the window function. Since each row of $W(k_i, k_j)$ is sharply peaked at $k_j \sim k_i$, the main contribution to $P_o(k_i)$ comes from modes near k_i ; therefore the constraints shown in Figure 6 depend weakly on the exact wave number range in which the model is computed, as long as it is larger than

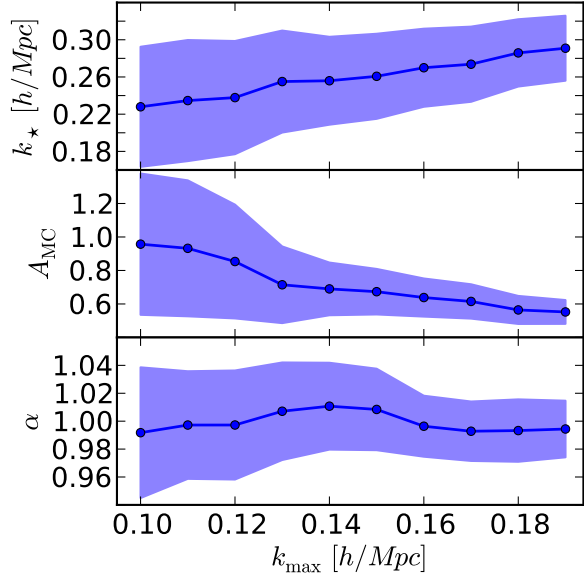


Figure 6. One-dimensional marginalised constraints on the parameters k_* , A_{MC} and α as function of the maximum value of k_i (k_{max}) used to fit the model of equation (3) to the LasDamas mean power spectrum. The mean values and the standard deviation are indicated, by circles connected with solid lines and shaded areas. The maximum value of k at which the model is computed before the convolution with the window function is $k = 0.2 \, h \, \text{Mpc}^{-1}$.

the range of the measured power spectrum that we fit. As k_{max} increases, more modes are included in the fit and the errors decrease. The constraints on α are compatible with unity for all the k_{max} considered. Considering that the volume of the simulations used in M10 is much larger than the one sampled by the LRGs and consequently that the errors in the former case are smaller than in the latter, we decide to further consider scales $0.02 \, h \, \text{Mpc}^{-1} \leq k \leq 0.15 \, h \, \text{Mpc}^{-1}$. The constraints on k_* and A_{MC} exhibit, respectively, a monotonic increase and decrease. As explained in M10, the approximate mode coupling power in equation (3) is about 30% larger than the exact value at $k \approx 0.15 - 0.2 \, h \, \text{Mpc}^{-1}$: this forces A_{MC} to decrease to $\sim 0.7 - 0.6$ and k_* to increase in order to maintain the shape of the resulting power spectrum unvaried.

Figure 7 shows the two-dimensional marginalised constraints in the $k_* - \alpha$ plane as obtained from the mock catalogues for $k_{\text{max}} = 0.15 \, h \, \text{Mpc}^{-1}$. The inner dark and outer light shaded areas represent regions whose volumes are 68% and 95% of the total likelihood. This representation of the two-dimensional constraints will be used through all section 6. The independence of α from k_* or A_{MC} makes the constraints on the former robust. The latter two parameters, instead, are strongly degenerate, as it is possible to describe accurately the overall shape of the power spectrum compensating an increase (decrease) of k_* with a decrease (increase) of A_{MC} .

The model power spectrum indicated by a solid line in the two panes of Figures 4 has been computed using the best fit values of the parameters as obtained in this section for $k_{\text{max}} = 0.15 \, h \, \text{Mpc}^{-1}$: $k_* = 0.26 \, h \, \text{Mpc}^{-1}$, $A_{\text{MC}} = 0.61$.

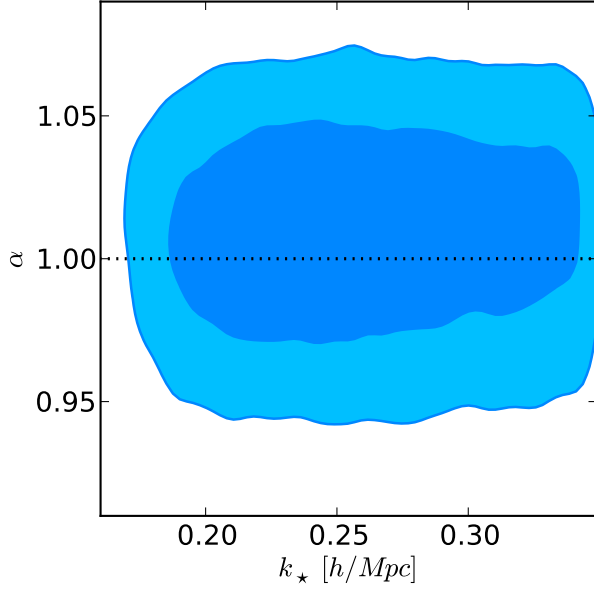


Figure 7. Two-dimensional marginalised constraints in the k_* – α plane obtained applying the model of equation (3) to the Las-Damas mean power spectrum. The results are shown for $k_{\max} = 0.15 h \text{ Mpc}^{-1}$. The inner dark and outer light areas represent the 68% and 95% confidence level, respectively.

The bias has been computed maximising the likelihood of equation (12) with all the other parameters fixed.

5.4.2 The Luminous red galaxy sample

After testing the robustness of our model at mildly non-linear scales, we test here the dependence of the cosmological parameters upon k_{\max} . We use the Λ CDM cosmology defined in equation (7) and the combination of the LRG power spectrum and CMB measurements. Figure 8 shows the one-dimensional marginalised constraints on the parameters ω_b , ω_{DM} , w_{DE} , Ω_{DE} , Ω_{M} , σ_8 and h as function of k_{\max} . The circles connected by solid lines and the shaded areas show the mean and the standard deviation as obtained from the MCMC. The model is computed for $k < 0.2 h \text{ Mpc}^{-1}$ and then convolved with the window function; as before, the measured parameters are mostly insensitive to this limit. Although some parameters are more stable with respect to changes of k_{\max} than others, there are no significant trends or deviations. The error-bars of the parameters decrease as k_{\max} increases: we interpret this as a sign of new information coming from these scales.

We also test the impact of using CMB measurements from WMAP only. We obtain the same constraints, but with errors larger by 5–10%, due to the loss of information at small angular scales, i.e. large multipoles l . Appendix B3 describes how the results just described depend upon p_w and w_i . A more extensive analysis of the Λ CDM cosmology is presented in section 6.3.

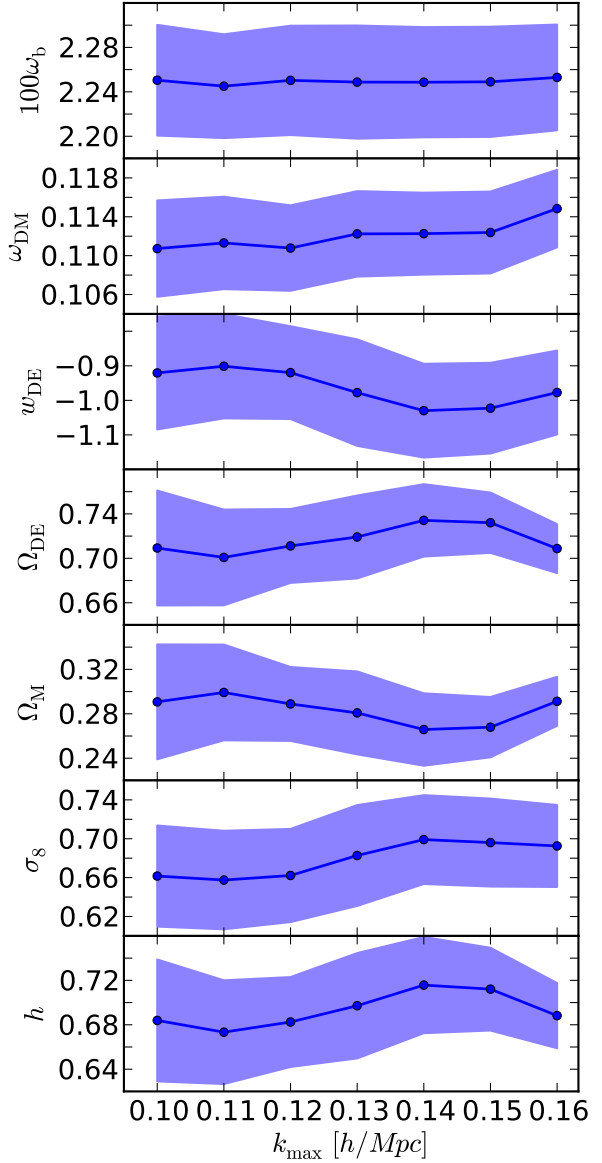


Figure 8. One-dimensional marginalised constraints of the Λ CDM parameter space on the parameters ω_b , ω_{DM} , w_{DE} , Ω_{DE} , Ω_{M} , σ_8 and h as function of the maximum value of k (k_{\max}) as obtained when combining the LRGs power spectrum with the CMB data. Circles connected by solid line and shaded areas are, respectively, the mean and the 68% confidence level. The model is computed for $k < 0.2 h \text{ Mpc}^{-1}$ and then convolved with the window function.

6 RESULTS: THE COSMOLOGICAL PARAMETERS

In this section we present the constraints on the cosmological parameters obtained from the five cosmological scenarios introduced in section 5.2.

6.1 The concordance cosmology

The flat Λ CDM cosmology, parametrized by the first six quantities of equation (5), is the minimal model able to describe data coming from many independent probes. Table 3

Table 3. Marginalised constraints on the cosmological parameters of the Λ CDM parameter space from the combination of probes listed in the header of the table. The quoted values are the means and widths of the posterior distribution containing 68% of the total area.

	CMB	CMB+ $P(k)$	CMB+ $P(k)$ + H_0	CMB+ $P(k)$ +SNIa	CMB+ $P(k)$ + H_0 +SNIa
$100\omega_b$	$2.254^{+0.052}_{-0.052}$	$2.258^{+0.048}_{-0.048}$	$2.259^{+0.050}_{-0.049}$	$2.252^{+0.047}_{-0.047}$	$2.260^{+0.047}_{-0.047}$
$100\omega_{DM}$	$10.96^{+0.52}_{-0.52}$	$11.23^{+0.36}_{-0.36}$	$11.10^{+0.35}_{-0.35}$	$11.22^{+0.34}_{-0.33}$	$11.13^{+0.33}_{-0.32}$
100Θ	$1.0400^{+0.0023}_{-0.0022}$	$1.0404^{+0.0020}_{-0.0020}$	$1.0406^{+0.0020}_{-0.0021}$	$1.0403^{+0.0021}_{-0.0020}$	$1.0406^{+0.0020}_{-0.0020}$
τ	$0.088^{+0.015}_{-0.015}$	$0.087^{+0.014}_{-0.014}$	$0.086^{+0.014}_{-0.014}$	$0.085^{+0.014}_{-0.015}$	$0.087^{+0.014}_{-0.014}$
n_s	$0.963^{+0.013}_{-0.013}$	$0.963^{+0.011}_{-0.012}$	$0.963^{+0.011}_{-0.011}$	$0.961^{+0.012}_{-0.011}$	$0.963^{+0.011}_{-0.011}$
$\log(10^{10} A_s)$	$3.065^{+0.033}_{-0.033}$	$3.075^{+0.031}_{-0.031}$	$3.068^{+0.033}_{-0.033}$	$3.070^{+0.032}_{-0.032}$	$3.071^{+0.032}_{-0.032}$
Ω_{DE}	$0.741^{+0.026}_{-0.026}$	$0.730^{+0.018}_{-0.018}$	$0.737^{+0.017}_{-0.017}$	$0.730^{+0.017}_{-0.017}$	$0.735^{+0.015}_{-0.016}$
Age [Gyr]	$13.722^{+0.111}_{-0.112}$	$13.723^{+0.094}_{-0.094}$	$13.711^{+0.095}_{-0.093}$	$13.735^{+0.094}_{-0.092}$	$13.710^{+0.091}_{-0.094}$
Ω_M	$0.259^{+0.026}_{-0.026}$	$0.270^{+0.018}_{-0.018}$	$0.263^{+0.017}_{-0.017}$	$0.270^{+0.017}_{-0.017}$	$0.265^{+0.016}_{-0.015}$
σ_8	$0.796^{+0.027}_{-0.027}$	$0.807^{+0.022}_{-0.022}$	$0.799^{+0.022}_{-0.022}$	$0.804^{+0.021}_{-0.021}$	$0.802^{+0.021}_{-0.021}$
z_{re}	$10.4^{+1.2}_{-1.2}$	$10.4^{+1.1}_{-1.2}$	$10.3^{+1.2}_{-1.2}$	$10.3^{+1.2}_{-1.2}$	$10.4^{+1.2}_{-1.2}$
H_0 [km s $^{-1}$ Mpc $^{-1}$]	$71.7^{+2.4}_{-2.3}$	$70.8^{+1.6}_{-1.6}$	$71.3^{+1.5}_{-1.5}$	$70.7^{+1.5}_{-1.5}$	$71.2^{+1.4}_{-1.4}$

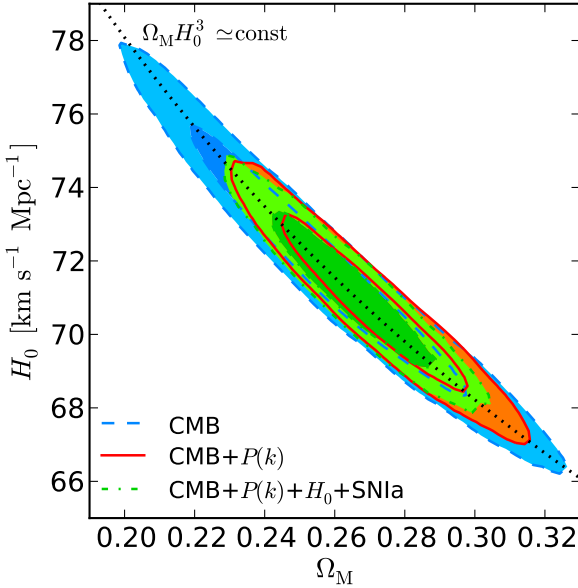


Figure 9. Two-dimensional marginalised constraints of the Λ CDM parameter space in the $\Omega_{DM} - H_0$ plane. Blue, red and green shaded areas enclosed in dashed, solid and dot-dashed lines shows the constraints from CMB alone, CMB+ $P_{LRG}(k)$ and CMB+ $P_{LRG}(k)$ + H_0 +SNIa, respectively. The inner darker and the outer lighter areas are the 68% and 95% confidence level. The black dotted line that runs across the figure shows the locus defined by equation $\Omega_M H_0^3 \simeq \text{const}$.

summarises the complete list of one-dimensional constraints for the primary and derived cosmological parameters obtained in this section. We quote the mean values and width of the posterior distribution containing 68% of the total area, which for a Gaussian distribution corresponds to the standard deviation, as obtained for the five different combinations of the four experiments used in this work. This convention will be followed in the rest of this article.

The CMB experiments described in section 4.1 provide measurements of the temperature and polarization angular power spectra with very high accuracy. The blue shaded areas enclosed in dashed lines in Figure 9 show the 68% and 95% confidence level in the $\Omega_{DM} - H_0$ as obtained when CMB information only is used. The apparent position of the peaks in the CMB power spectra is proportional to their physical scale, which depends on the composition of the early universe (baryons, dark matter and radiation), and the angular diameter distance to the last scattering surface, a function of H_0 and of the density and equation of state parameter of matter, dark energy and of curvature. Since here we consider a flat geometry and fix w_{DE} to -1, a degeneracy between the matter density and the Hubble parameter appears. It has been shown by Percival et al. (2002) that this effect, together with the preservation of the relative amplitude of the peaks, leads, in a Λ CDM universe, to a degeneracy along the curve defined by $\Omega_M h^3 \simeq \text{const}$, which is displayed in Figure 9 by the dotted line. The accurate detection of the third peak in the temperature power spectrum, whose relative amplitude with respect to the first two is proportional to the matter-radiation ratio, helps reducing this degeneracy. In this case we measure $\Omega_M = 0.259 \pm 0.026$, $H_0 = 71.7^{+2.4}_{-2.3}$ km s $^{-1}$ Mpc $^{-1}$ and $\omega_{DM} = (10.96 \pm 0.52) \times 10^{-2}$.

The inclusion of information from the large scale structure can break or reduce some of the degeneracies in the CMB. The shape of the power spectrum depends upon $\Omega_M h$ and, more weakly, Ω_b/Ω_M (e.g., Efstathiou et al. 2002; Sánchez & Cole 2008). Thanks to this, the errors on the cosmological parameters decrease up to about 30%. In particular, we measure a decrease in the allowed region by about one third in the three parameters considered before: $\Omega_M = 0.27 \pm 0.018$, $H_0 = 70.8 \pm 1.6$ km s $^{-1}$ Mpc $^{-1}$ and $\omega_{DM} = (11.23^{+0.36}_{-0.36}) \times 10^{-2}$. The two-dimensional constraints in the $\Omega_M - H_0$ plane are shown in Figure 9 with the red shaded areas within solid lines.

When the SNIa and H_0 measurements are also used, we obtain $\Omega_M = 0.265^{+0.016}_{-0.015}$, $H_0 = 71.2 \pm 1.4$ km s $^{-1}$ Mpc $^{-1}$

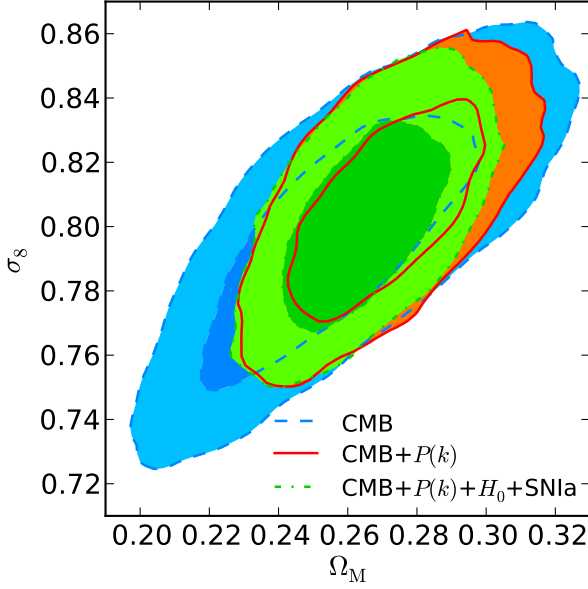


Figure 10. Two-dimensional marginalised constraints of the Λ CDM parameter space in the $\Omega_m - \sigma_8$ plane. The colour and line coding is the same as in Figure 9.

and $\omega_{DM} = (11.13^{+0.33}_{-0.32}) \times 10^{-2}$, which means a 10-15% increase in accuracy. The two dimensional 68% and 95% confidence levels for the former two parameters, when all the four probes are used, are shown in Figure 9 by the green shaded areas enclosed by dot-dashed lines.

Figure 10 shows the two-dimensional marginalised constraints in the $\Omega_M - \sigma_8$ plane for the same combination of datasets; colour and line coding is the same as in Figure 9. The correlation between the two parameters is caused by the fact that an increase (decrease) of Ω_M causes a decrease (increase) in the amplitude of the power spectrum that can be compensated by a larger (smaller) value of σ_8 . For the three cases shown in the figure we find that the one-dimensional constraints on the latter parameter are, respectively, $\sigma_8 = 0.796 \pm 0.027$, $\sigma_8 = 0.807 \pm 0.022$ and $\sigma_8 = 0.802 \pm 0.021$; the error on the latter two decreases by 20 and 22% respectively to the CMB only result.

The solid lines in Figures 2 and 3 show the model power spectrum computed using the cosmological parameters listed in the last column of Table 3 and the best fit model parameters $k_* = 0.28 h \text{ Mpc}^{-1}$ and $A_{MC} = 0.72$, as obtained from the MCMC for $k_{max} = 0.15 h \text{ Mpc}^{-1}$. The bias has been computed maximising the likelihood of equation (12) with all the other parameters fixed.

Effects of supernovae systematics and light curve fitters

Uncertainties in the modelling of SNIa can affect the cosmological parameters and associated errors extracted using a given dataset. To test the impact of systematics and light curve fitters on the results just presented, we re-analyse the Λ CDM cosmology with two different SNIa settings. First we use the same Union2 set, but neglecting the systematic errors provided with the data; second we substitute this dataset with the Sloan Digital Sky Survey-II Supernova Survey sample (SDSS SN, Kessler et al. 2009). The sam-

Table 4. Marginalised constraints on the cosmological parameters of the Λ CDM parameter space from the combination of CMB+ $P_{LRG}(k)$ + H_0 +SNIa when systematic errors are not considered and when the MLCS2k2 SNIa light curve fitter is used.

	no systematics	MLCS2k2
$100\omega_b$	$2.258^{+0.046}_{-0.048}$	$2.244^{+0.047}_{-0.046}$
$100\omega_{DM}$	$11.16^{+0.28}_{-0.29}$	$11.61^{+0.31}_{-0.31}$
100Θ	$1.0405^{+0.0020}_{-0.0020}$	$1.0402^{+0.0021}_{-0.0020}$
τ	$0.087^{+0.014}_{-0.014}$	$0.084^{+0.014}_{-0.014}$
n_s	$0.963^{+0.011}_{-0.011}$	$0.957^{+0.011}_{-0.011}$
$\log(10^{10} A_s)$	$3.072^{+0.033}_{-0.033}$	$3.081^{+0.031}_{-0.032}$
Ω_{DE}	$0.734^{+0.013}_{-0.013}$	$0.709^{+0.016}_{-0.016}$
Age [Gyr]	$13.717^{+0.089}_{-0.089}$	$13.765^{+0.090}_{-0.090}$
Ω_M	$0.266^{+0.013}_{-0.013}$	$0.291^{+0.016}_{-0.016}$
σ_8	$0.803^{+0.020}_{-0.020}$	$0.822^{+0.021}_{-0.021}$
z_{re}	$10.4^{+1.2}_{-1.2}$	$10.3^{+1.2}_{-1.2}$
$H_0 [\text{km s}^{-1} \text{ Mpc}^{-1}]$	$71.0^{+1.2}_{-1.2}$	$69.1^{+1.3}_{-1.3}$

ple consists of 288 supernovae from 5 different experiments whose light curves have been fitted both with the MLCS2k2 (Jha, Riess & Kirshner 2007) and SALT2 models. Since most of the objects in SDSS SN are also part of the Union2, we do not expect large differences between the two samples if SALT2 is used. Therefore we show here only the results obtained using the MLCS2k2 fitter. The one-dimensional constraints that we extract from the combination of all four probes, when the systematics in the Union2 are ignored and when the SDSS SN with MLCS2k2 are used, are listed in Table 4. As expected, and in agreement with Amanullah et al. (2010), ignoring systematic errors globally reduces the errors on the recovered values of the parameters without changing sensibly the mean value. As example we obtain $\Omega_M = 0.266 \pm 0.013$ (14% decrease with respect to the corresponding case in Table 3), $H_0 = 71 \pm 1.2 \text{ km s}^{-1} \text{ Mpc}^{-1}$ (12%), $\omega_{DM} = (11.16^{+0.28}_{-0.29}) \times 10^{-2}$ (14%) and $\sigma_8 = 0.803 \pm 0.02$ (5%). On the other hand, the use of MLCS2k2 changes the posterior distribution sensibly, without influencing its width. We measure that Ω_M , ω_{DM} and H_0 change by more than 1.5-2 σ . This shift agrees with the findings in Kessler et al. (2009) and Bengochea (2011) and suggests, in our opinion, that the choice of the model used to fit the light curves can bias sensibly the cosmological results obtained.

6.2 Curvature

In this section we analyse the cosmological constraints obtained when the curvature is considered as a free parameter. The full list of parameters (mean plus the 68% confidence level) is shown in Table 5 for the combination of experiments listed in the header of the table.

The blue shaded areas within dashed lines in panel a) of Figure 11 and in Figure 12 show the two-dimensional marginalised constraints in the $\Omega_{DE} - \Omega_M$ and $\Omega_{DE} - H_0$ planes, respectively, as obtained from CMB data alone. The

Table 5. Marginalised constraints on the cosmological parameters of the Λ CDM parameter space from the combination of probes listed in the header of the table. The quoted values are the same as in Table 3.

	CMB	CMB+ $P(k)$	CMB+ $P(k)$ + H_0	CMB+ $P(k)$ +SNIa	CMB+ $P(k)$ + H_0 +SNIa
$100\omega_b$	$2.232^{+0.052}_{-0.050}$	$2.250^{+0.048}_{-0.047}$	$2.252^{+0.050}_{-0.049}$	$2.245^{+0.050}_{-0.048}$	$2.247^{+0.049}_{-0.050}$
$100\omega_{DM}$	$11.06^{+0.50}_{-0.50}$	$11.29^{+0.44}_{-0.45}$	$11.30^{+0.45}_{-0.45}$	$11.30^{+0.42}_{-0.41}$	$11.31^{+0.43}_{-0.44}$
100Θ	$1.0396^{+0.0022}_{-0.0022}$	$1.0401^{+0.0022}_{-0.0021}$	$1.0402^{+0.0022}_{-0.0022}$	$1.0400^{+0.0021}_{-0.0021}$	$1.0400^{+0.0022}_{-0.0021}$
τ	$0.086^{+0.014}_{-0.015}$	$0.085^{+0.014}_{-0.014}$	$0.085^{+0.014}_{-0.014}$	$0.085^{+0.014}_{-0.014}$	$0.085^{+0.015}_{-0.014}$
$100\Omega_k$	$-4.90^{+4.39}_{-5.10}$	$0.16^{+0.54}_{-0.54}$	$0.30^{+0.49}_{-0.49}$	$0.14^{+0.51}_{-0.53}$	$0.30^{+0.48}_{-0.47}$
n_s	$0.956^{+0.013}_{-0.013}$	$0.961^{+0.012}_{-0.012}$	$0.961^{+0.012}_{-0.012}$	$0.960^{+0.012}_{-0.012}$	$0.960^{+0.012}_{-0.012}$
$\log(10^{10} A_s)$	$3.062^{+0.033}_{-0.033}$	$3.072^{+0.030}_{-0.031}$	$3.073^{+0.032}_{-0.032}$	$3.072^{+0.032}_{-0.032}$	$3.073^{+0.033}_{-0.033}$
Ω_{DE}	$0.597^{+0.132}_{-0.149}$	$0.731^{+0.019}_{-0.019}$	$0.730^{+0.016}_{-0.016}$	$0.730^{+0.016}_{-0.016}$	$0.734^{+0.015}_{-0.015}$
Age [Gyr]	$15.37^{+1.46}_{-1.37}$	$13.65^{+0.27}_{-0.27}$	$13.58^{+0.23}_{-0.24}$	$13.67^{+0.26}_{-0.26}$	$13.59^{+0.24}_{-0.24}$
Ω_M	$0.452^{+0.200}_{-0.175}$	$0.267^{+0.020}_{-0.021}$	$0.261^{+0.017}_{-0.017}$	$0.269^{+0.018}_{-0.017}$	$0.263^{+0.016}_{-0.015}$
σ_8	$0.773^{+0.032}_{-0.032}$	$0.808^{+0.024}_{-0.025}$	$0.809^{+0.026}_{-0.026}$	$0.808^{+0.025}_{-0.025}$	$0.810^{+0.025}_{-0.026}$
z_{re}	$10.3^{+1.2}_{-1.2}$	$10.3^{+1.2}_{-1.1}$	$10.3^{+1.2}_{-1.2}$	$10.3^{+1.2}_{-1.1}$	$10.4^{+1.2}_{-1.2}$
H_0 [km s $^{-1}$ Mpc $^{-1}$]	$57.3^{+11.5}_{-12.0}$	$71.3^{+2.5}_{-2.4}$	$72.1^{+2.1}_{-2.0}$	$71.1^{+2.2}_{-2.2}$	$71.9^{+1.9}_{-2.0}$

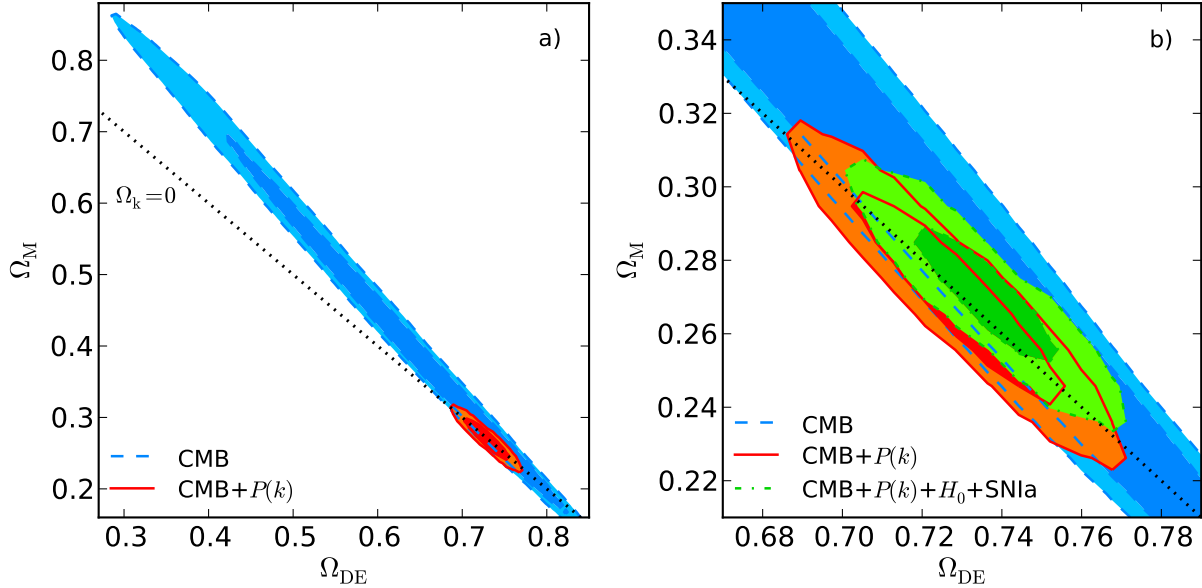


Figure 11. Two-dimensional marginalised constraints of the Λ CDM parameter space in the $\Omega_{DE} - \Omega_M$ plane. Panel *b*) zooms into panel *a*) in order to highlight the constraints obtained when combining CMB with the other datasets used in this work. The diagonal dotted line is for a flat Universe. Colour and line coding is the same as in Figure 9.

plots show a very strong degeneracy between these parameters. As stated in Section 6.1, the apparent size of the CMB acoustic peaks depends on their physical size and the angular diameter distance. Given that curvature density is small and that it scales as the inverse square of the scale factor, it affects much more D_A than the dynamics of the early universe. It is always possible to find combinations of Ω_k , ω_m and ω_b that keeps the angular size of the CMB peaks constant. Therefore, the constraints on the derived parameters are much weaker than the ones obtained in the previous section: $\Omega_{DE} = 0.6^{+0.13}_{-0.15}$, $\Omega_M = 0.45^{+0.20}_{-0.17}$ and $H_0 = 57^{+11}_{-12}$ km s $^{-1}$ Mpc $^{-1}$. The measured curvature,

$\Omega_k = (-4.9^{+4.4}_{-5.1}) \times 10^{-2}$, is compatible with flatness at about the 1σ level.

Both panels in Figure 11 and Figure 12 show, with red shaded areas enclosed in solid lines, the same parameter planes as above when explored combining CMB and large scale structure information. Panel *b*) of Figure 11 shows a zoom of the constraints of panel *a*) in the area around $\Omega_{DE} = 0.73$ and $\Omega_M = 0.28$ in order to show with more details the constraints obtained when more information is added to the CMB data. The galaxy power spectrum is very sensitive to the matter density. Additionally the BAOs allow to measure the angular diameter distance to the mean redshift of the

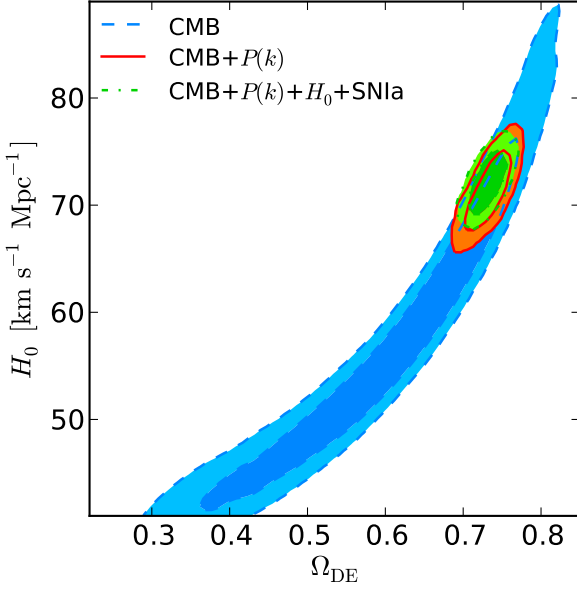


Figure 12. Two-dimensional marginalised constraints of the Λ CDM parameter space in the $\Omega_{\text{DE}} - H_0$ plane. Colour and line coding is the same as in Figure 9.

LRG sample, $\bar{z} = 0.313$. The degeneracies in the CMB alone are therefore strongly reduced when LSS measurements are included. The four variables discussed in the previous paragraphs become $\Omega_{\text{DE}} = 0.731 \pm 0.019$, $\Omega_{\text{M}} = 0.267^{+0.020}_{-0.021}$, $H_0 = 71.3 \pm 2.5$ and $\Omega_{\text{k}} = (1.6 \pm 5.4) \times 10^{-3}$: their errors are almost one order of magnitude smaller than in the CMB only case. With respect to the corresponding Λ CDM case, the uncertainties on the first three quantities increase up to 50%.

The inclusion of SNIa and H_0 measurement, decreases the errors on curvature by about 10% ($\Omega_{\text{k}} = [3^{+4.8}_{-4.7}] \times 10^{-3}$) and on the other three parameters considered before by circa 20% ($\Omega_{\text{DE}} = 0.734^{+0.015}_{-0.015}$, $\Omega_{\text{M}} = 0.263^{+0.016}_{-0.015}$ and $H_0 = 71.9^{+1.9}_{-2.0}$). When comparing with the results from the previous section, the errors on dark energy and matter density are unchanged, while increasing by less than 40% for the Hubble parameters. The two-dimensional marginalised constraints in the $\Omega_{\text{DE}} - \Omega_{\text{M}}$ and $\Omega_{\text{DE}} - H_0$ planes are shown in panel b) of Figure 11 and in Figure 12 with green shaded lines enclosed in dot-dashed lines.

6.3 Beyond the cosmological constant

In sections 6.1 and 6.2 we assume that dark energy is modelled as a cosmological constant. Despite its simplicity and its success in describing simultaneously many independent observations, the present day value of the density of dark energy does not have a solid physical explanation; this led, in the past decade, to the exploration of a large number of alternative model, most of which present a time dependent equation of state⁶. Ideally, one would like to be able to constrain the full time, or redshift, dependence of $w_{\text{DE}}(z)$ in order to restrict the range of possible models. Usually,

⁶ All theories of modified gravity can be also represented through an effective $w_{\text{DE}}(z)$.

parametric forms for the dark energy equation of state are assumed, which allow to measure time dependencies, but do not necessarily reproduce the correct $w_{\text{DE}}(z)$. With non-parametric approaches and principal component analysis it is possible to overcome some of these limitations (e.g., Huterer & Starkman 2003; Serra et al. 2009; Holsclaw et al. 2010). In this section we assume the simplest parametric form possible: w_{DE} is a constant, independent of time, with a flat prior in the range $[-2, 0]$. Deviations from the value $w_{\text{DE}} = -1$ would suggest that the cosmological constant is not a viable model of dark energy. If this is the case, the results shown in the previous two sections could be biased as consequence of wrongly assuming that dark energy is described by Λ . In section 6.5 we analyse an alternative scenario in which w_{DE} is parametrized as a linear function of the scale factor.

Table 6 lists the constraints on the cosmological parameters as obtained for the different combinations of datasets analysed in this work. They are in perfect agreement with the ones presented with the previous two parameter spaces.

Panel a) of Figure 13 shows the constraints in the $\Omega_{\text{DE}} - w_{\text{DE}}$ plane. The horizontal dotted line corresponds to $w_{\text{DE}} = -1$. If the CMB alone is considered a strong degeneracy between these two parameters is present, as shown by blue shaded areas enclosed by dashed lines. The reason for this degeneracy is analogous to the case analysed in the previous section when curvature is left as free parameter. In fact, while dark energy is subdominant at early times and does not influence the physical scale of the acoustic peaks, its equation of state parameter and density have a strong effect on the angular diameter distance to the last scattering surface. Thus different combinations of ω_{DM} , ω_{b} and w_{DE} can result in the same apparent position of the acoustic oscillations in the CMB temperature power spectrum. The constraints on the dark energy density and equation of state parameter are therefore very weak: $\Omega_{\text{DE}} = 0.64^{+0.12}_{-0.13}$ and $w_{\text{DE}} = -0.74^{+0.32}_{-0.30}$.

With the inclusion of the LRGs data, the degeneracies in the CMB are broken, as shown in the panel a) of Figure 13 (solid line enclosing red areas). From the same figure it is clear that the impact of supernovae and H_0 (dot-dashed line enclosing green areas) information is much larger in this scenario than in the previous two. In order to understand what causes such a difference, we show in panel b) of Figure 13 also the two dimensional constraints obtained from the combination of CMB+ $P_{\text{LRG}}(k)$ +SNIa (dashed lines enclosing blue areas). The horizontal line corresponds to $w_{\text{DE}} = -1$. The plot shows clearly that supernovae have a large constraining power for this parameter space. In fact the supernovae luminosity-distance relation traces the expansion history of the Universe and clearly identifies the transition between the deceleration and acceleration phases (Riess et al. 2004). This transition depends on the densities of the cosmic components and is very sensitive to the dark energy equation of state. The inclusion of a precise measurement of H_0 increases the precision on the parameters by a small factor. The constraints on the dark energy equation of state are i) $w_{\text{DE}} = -1.02 \pm 0.13$, from CMB+ $P_{\text{LRG}}(k)$, ii) $w_{\text{DE}} = -1.07 \pm 0.11$, from CMB+ $P_{\text{LRG}}(k)$ + H_0 , iii) $w_{\text{DE}} = -1.009 \pm 0.069$, CMB+ $P_{\text{LRG}}(k)$ +SNIa and iv) $w_{\text{DE}} = -1.025^{+0.066}_{-0.065}$, from CMB+ $P_{\text{LRG}}(k)$ + H_0 +SNIa. Therefore the inclusion of

Table 6. Marginalised constraints on the cosmological parameters of the w CDM parameter space from the combination of probes listed in the header of the table. The quoted values are the same as in Table 3.

	CMB	CMB+ $P(k)$	CMB+ $P(k)+H_0$	CMB+ $P(k)+\text{SNIa}$	CMB+ $P(k)+H_0+\text{SNIa}$
$100\omega_b$	$2.242^{+0.053}_{-0.054}$	$2.251^{+0.049}_{-0.050}$	$2.256^{+0.049}_{-0.049}$	$2.250^{+0.051}_{-0.052}$	$2.257^{+0.048}_{-0.050}$
$100\omega_{\text{DM}}$	$11.01^{+0.53}_{-0.53}$	$11.25^{+0.43}_{-0.43}$	$11.28^{+0.44}_{-0.44}$	$11.26^{+0.40}_{-0.41}$	$11.25^{+0.40}_{-0.40}$
100Θ	$1.0397^{+0.0023}_{-0.0022}$	$1.0402^{+0.0022}_{-0.0022}$	$1.0403^{+0.0021}_{-0.0021}$	$1.0403^{+0.0021}_{-0.0021}$	$1.0404^{+0.0020}_{-0.0020}$
τ	$0.088^{+0.015}_{-0.015}$	$0.086^{+0.015}_{-0.015}$	$0.087^{+0.014}_{-0.014}$	$0.086^{+0.015}_{-0.014}$	$0.086^{+0.014}_{-0.014}$
w_{DE}	$-0.742^{+0.324}_{-0.303}$	$-1.022^{+0.129}_{-0.128}$	$-1.069^{+0.107}_{-0.106}$	$-1.009^{+0.069}_{-0.069}$	$-1.025^{+0.066}_{-0.065}$
n_s	$0.959^{+0.014}_{-0.014}$	$0.962^{+0.012}_{-0.012}$	$0.962^{+0.012}_{-0.012}$	$0.961^{+0.012}_{-0.012}$	$0.963^{+0.012}_{-0.012}$
$\log(10^{10} A_s)$	$3.064^{+0.032}_{-0.033}$	$3.073^{+0.034}_{-0.033}$	$3.076^{+0.033}_{-0.032}$	$3.073^{+0.032}_{-0.032}$	$3.074^{+0.032}_{-0.031}$
Ω_{DE}	$0.637^{+0.123}_{-0.133}$	$0.732^{+0.028}_{-0.028}$	$0.743^{+0.020}_{-0.020}$	$0.729^{+0.018}_{-0.018}$	$0.735^{+0.015}_{-0.016}$
Age [Gyr]	$14.062^{+0.431}_{-0.396}$	$13.733^{+0.118}_{-0.117}$	$13.692^{+0.095}_{-0.099}$	$13.736^{+0.102}_{-0.102}$	$13.713^{+0.090}_{-0.089}$
Ω_{M}	$0.363^{+0.133}_{-0.123}$	$0.268^{+0.028}_{-0.028}$	$0.257^{+0.020}_{-0.020}$	$0.271^{+0.018}_{-0.018}$	$0.265^{+0.016}_{-0.015}$
σ_8	$0.726^{+0.085}_{-0.090}$	$0.818^{+0.065}_{-0.064}$	$0.838^{+0.059}_{-0.060}$	$0.810^{+0.042}_{-0.043}$	$0.817^{+0.043}_{-0.042}$
z_{re}	$10.6^{+1.2}_{-1.2}$	$10.4^{+1.2}_{-1.2}$	$10.4^{+1.1}_{-1.1}$	$10.4^{+1.2}_{-1.2}$	$10.3^{+1.2}_{-1.2}$
H_0 [km s $^{-1}$ Mpc $^{-1}$]	$63.1^{+10.6}_{-11.2}$	$71.2^{+3.8}_{-3.8}$	$72.8^{+2.8}_{-2.8}$	$70.7^{+2.0}_{-2.0}$	$71.4^{+1.7}_{-1.7}$

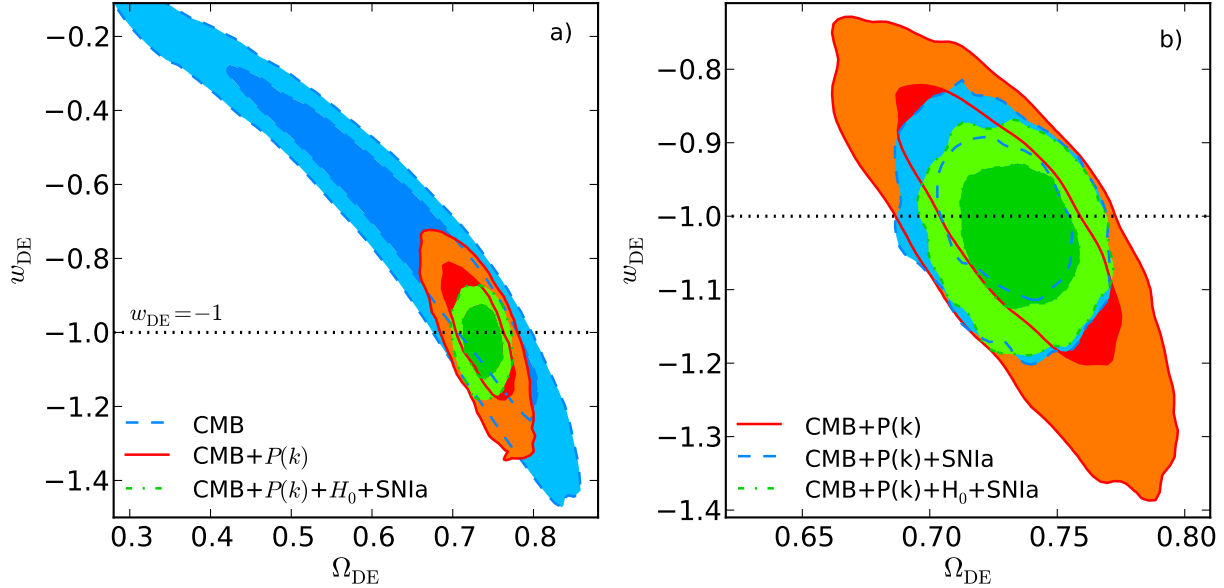


Figure 13. Panel *a*): two-dimensional marginalised constraints of the w CDM parameter space in the $w_{\text{DE}} - \Omega_{\text{DE}}$ plane. Colour and line coding is the same as in Figure 9. Panel *b*): same as the upper panel, but for CMB+ $P_{\text{LRG}}(k)$, red areas within solid lines, CMB+ $P_{\text{LRG}}(k)+\text{SNIa}$, blue areas within dashed lines, and CMB+ $P_{\text{LRG}}(k)+H_0+\text{SNIa}$, green areas within dot-dashed lines. Note that the lower panel is a zoom of the upper one in the region occupied by the CMB+ $P_{\text{LRG}}(k)$ contours. The dotted horizontal line shows $w_{\text{DE}} = -1$

the large scale structure measurements decreases the error on w_{DE} by about a factor 3 and SNIa further halve it.

The main result of this section is that, when combining CMB, LSS, SNIa information with the prior on H_0 , the equation of state parameter of dark energy is constrained to be -1 with about 6.5% accuracy. This, although perfectly compatible with the cosmological constant models, does not exclude other dark energy scenarios. Excluding CMB, which has very little constraining power, the other three experiments give us access only to redshift $z \gtrsim 1$. Furthermore

many dark energy models can be tuned in order to mimic Λ at low redshifts and deviate from it at earlier epochs. In order to narrow the range of possible models, more precise measurements spanning a larger range of redshifts, together with the inclusion of tests of the growth of structures, will be necessary.

Table 7. Marginalised constraints on the cosmological parameters of the w CDM parameter space from the combination of CMB+ $P_{\text{LRG}}(k)$ + H_0 +SNIa when systematic errors are not considered and when the MLCS2K2 SNIa light curve fitter is used.

	no systematics	MLCS2K2
$100\omega_b$	$2.257^{+0.047}_{-0.048}$	$2.264^{+0.048}_{-0.049}$
$100\omega_{\text{DM}}$	$11.21^{+0.40}_{-0.40}$	$11.05^{+0.41}_{-0.41}$
100Θ	$1.0405^{+0.0021}_{-0.0021}$	$1.0411^{+0.0021}_{-0.0022}$
τ	$0.087^{+0.014}_{-0.014}$	$0.089^{+0.014}_{-0.014}$
w_{DE}	$-1.007^{+0.046}_{-0.046}$	$-0.875^{+0.054}_{-0.055}$
n_s	$0.962^{+0.012}_{-0.012}$	$0.964^{+0.012}_{-0.012}$
$\log(10^{10} A_s)$	$3.074^{+0.032}_{-0.032}$	$3.072^{+0.032}_{-0.033}$
Ω_{DE}	$0.732^{+0.013}_{-0.014}$	$0.704^{+0.017}_{-0.017}$
Age [Gyr]	$13.719^{+0.091}_{-0.090}$	$13.795^{+0.095}_{-0.093}$
Ω_{M}	$0.268^{+0.014}_{-0.013}$	$0.296^{+0.017}_{-0.017}$
σ_8	$0.809^{+0.036}_{-0.036}$	$0.752^{+0.037}_{-0.037}$
z_{re}	$10.4^{+1.2}_{-1.1}$	$10.5^{+1.1}_{-1.2}$
$H_0 [\text{km s}^{-1} \text{Mpc}^{-1}]$	$71.0^{+1.2}_{-1.2}$	$67.2^{+1.5}_{-1.5}$

Effects of supernovae systematics and light curve fitters

Similarly to what has been done in section 6.1, we test the impact of SNIa systematic effects and different light curve fitters on the measured cosmological parameters. The constraints for these two cases are listed in Table 7. As before, we find that neglecting systematics does not change the mean values of the parameters, but generally reduces the associated errors. In particular the constraints on the dark energy equation of state are reduced by almost 30%, $w_{\text{DE}} = -1.007 \pm 0.046$. The use of the data from the SDSS SN project, with the light curves fitted with MLCS2K2, changes some of the parameters, as for instance H_0 , w_{DE} and Ω_{M} , by more than 2- σ with respect to the value in our standard case. In particular we measure w_{DE} to be $-0.875^{+0.054}_{-0.055}$. This highlights, better than for the Λ CDM case, the importance of SNIa modelling in improving cosmological constraints from future generation experiments.

6.4 Curvature and dark energy equation of state as free parameters

We now analyse the accuracy that can be achieved when both w_{DE} and Ω_k are considered as free parameters. The full list of constraints on the cosmological parameters for the kwCDM cosmology is summarised in Table 8.

The introduction of an extra degree of freedom with respect to the previous two sections affects the CMB degeneracy already discussed. The two-dimensional marginalised constraints in the $w_{\text{DE}} - \Omega_k$ and $w_{\text{DE}} - \Omega_{\text{DE}}$ planes from CMB data only are shown in Figures 14 and 15 with the blue shaded areas within dashed lines. By comparing Figure 15 with panel a) of Figure 13 it becomes clear that the allowed area in the parameter space increases because of the larger degeneracy. This causes the errors on Ω_k and w_{DE} to

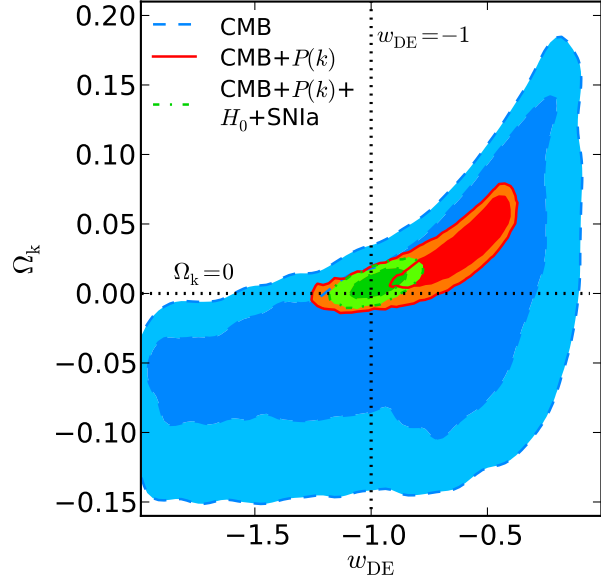


Figure 14. Two-dimensional marginalised constraints of the kwCDM parameter space in the $w_{\text{DE}} - \Omega_k$ plane. Colour and line coding is the same as in Figure 9. The horizontal and vertical dotted lines show the values of these parameters for the flat Λ CDM case.

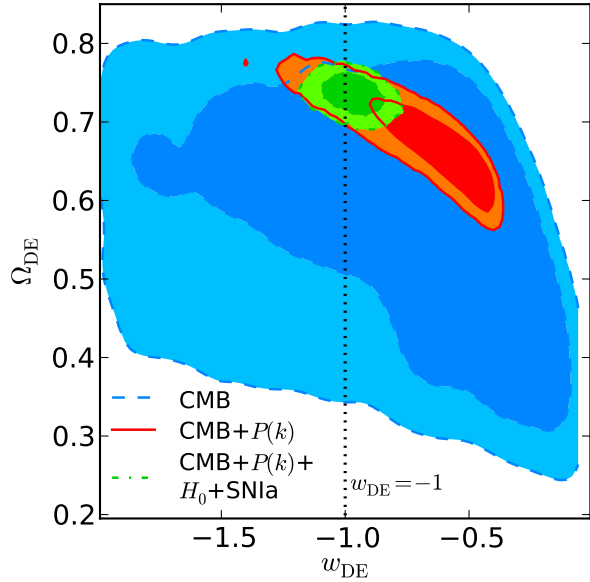


Figure 15. Two-dimensional marginalised constraints of the kwCDM parameter space in the $w_{\text{DE}} - \Omega_{\text{DE}}$ plane. Colour and line coding is the same as in Figure 9. The vertical dotted line shows $w_{\text{DE}} = -1$

increase by 50-60% with respect to the corresponding cases in sections 6.2 and 6.3.

The red contours within solid lines in Figures 14 and 15 show the constraints in the $w_{\text{DE}} - \Omega_k$ and $w_{\text{DE}} - \Omega_{\text{DE}}$ planes from the combination of CMB with the LRG data. The inclusion of the power spectrum reduces the region allowed by CMB alone to a one-dimensional degeneracy, that can be broken using the information on the amplitude of

Table 8. Marginalised constraints on the cosmological parameters of the Λ CDM parameter space from the combination of probes listed in the header of the table. The quoted values are the same as in Table 3.

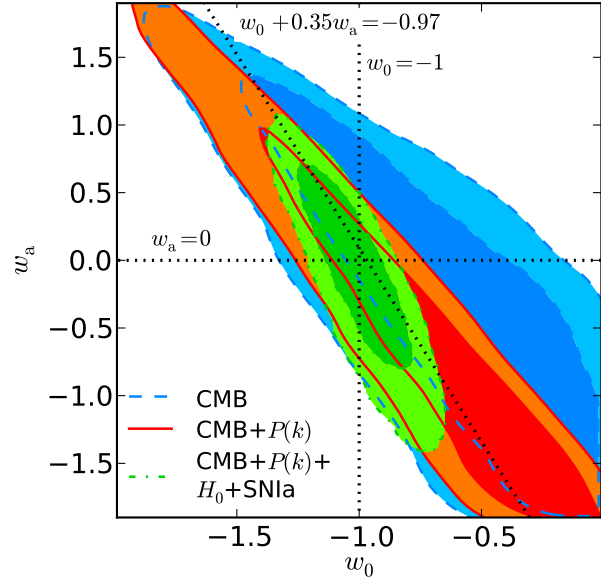
	CMB	CMB+ $P(k)$	CMB+ $P(k)$ + H_0	CMB+ $P(k)$ +SNIa	CMB+ $P(k)$ + H_0 +SNIa
$100\omega_b$	$2.236^{+0.052}_{-0.052}$	$2.241^{+0.047}_{-0.047}$	$2.255^{+0.048}_{-0.048}$	$2.246^{+0.047}_{-0.047}$	$2.251^{+0.050}_{-0.049}$
$100\omega_{DM}$	$11.04^{+0.52}_{-0.52}$	$11.29^{+0.43}_{-0.44}$	$11.32^{+0.46}_{-0.45}$	$11.27^{+0.43}_{-0.43}$	$11.30^{+0.45}_{-0.46}$
100Θ	$1.0397^{+0.0022}_{-0.0022}$	$1.0400^{+0.0020}_{-0.0021}$	$1.0401^{+0.0021}_{-0.0021}$	$1.0401^{+0.0022}_{-0.0022}$	$1.0402^{+0.0021}_{-0.0022}$
τ	$0.087^{+0.014}_{-0.014}$	$0.086^{+0.014}_{-0.014}$	$0.087^{+0.015}_{-0.015}$	$0.086^{+0.014}_{-0.014}$	$0.085^{+0.014}_{-0.014}$
$100\Omega_k$	$-2.72^{+6.28}_{-6.51}$	$2.72^{+2.18}_{-2.13}$	$1.69^{+2.11}_{-1.92}$	$0.33^{+0.71}_{-0.72}$	$0.45^{+0.65}_{-0.65}$
w_{DE}	$-0.907^{+0.524}_{-0.607}$	$-0.685^{+0.200}_{-0.207}$	$-0.856^{+0.262}_{-0.272}$	$-0.973^{+0.091}_{-0.088}$	$-0.981^{+0.083}_{-0.084}$
n_s	$0.956^{+0.013}_{-0.013}$	$0.959^{+0.012}_{-0.012}$	$0.962^{+0.012}_{-0.012}$	$0.960^{+0.012}_{-0.012}$	$0.961^{+0.012}_{-0.012}$
$\log(10^{10} A_s)$	$3.063^{+0.033}_{-0.032}$	$3.074^{+0.032}_{-0.032}$	$3.077^{+0.032}_{-0.033}$	$3.072^{+0.032}_{-0.032}$	$3.073^{+0.031}_{-0.032}$
Ω_{DE}	$0.566^{+0.139}_{-0.153}$	$0.671^{+0.047}_{-0.045}$	$0.710^{+0.042}_{-0.043}$	$0.728^{+0.017}_{-0.017}$	$0.733^{+0.016}_{-0.017}$
Age [Gyr]	$15.01^{+1.78}_{-1.88}$	$13.11^{+0.47}_{-0.45}$	$13.24^{+0.57}_{-0.58}$	$13.61^{+0.33}_{-0.32}$	$13.53^{+0.29}_{-0.29}$
Ω_M	$0.461^{+0.197}_{-0.176}$	$0.302^{+0.030}_{-0.031}$	$0.273^{+0.026}_{-0.026}$	$0.268^{+0.017}_{-0.017}$	$0.262^{+0.016}_{-0.016}$
σ_8	$0.725^{+0.109}_{-0.117}$	$0.692^{+0.080}_{-0.077}$	$0.757^{+0.106}_{-0.102}$	$0.797^{+0.044}_{-0.045}$	$0.802^{+0.044}_{-0.043}$
z_{re}	$10.6^{+1.3}_{-1.3}$	$10.7^{+1.2}_{-1.2}$	$10.6^{+1.2}_{-1.2}$	$10.4^{+1.2}_{-1.1}$	$10.4^{+1.2}_{-1.2}$
H_0 [km s $^{-1}$ Mpc $^{-1}$]	$56.7^{+11.2}_{-11.5}$	$67.2^{+3.4}_{-3.3}$	$70.8^{+3.2}_{-3.2}$	$71.0^{+2.2}_{-2.2}$	$71.9^{+2.0}_{-2.0}$

$P_{LRG}(k)$. Therefore a degeneracy arises between the bias and the shape of the power spectrum when both the curvature and the dark energy equation of state are treated as free parameters. When considering the range of scales $0.02 h \text{ Mpc}^{-1} \leq k \leq 0.15 h \text{ Mpc}^{-1}$ larger values of w_{DE} , Ω_M and Ω_k and lower values of σ_8 can be compensated by unphysically large biases b and larger values of A_{MC} in order to obtain a comparable χ^2 . If we used a finite flat prior on b we would decrease the large Ω_k and w_{DE} tail and reduce the degeneracy. Alternatively, the detection of the turnover in the power spectrum, not possible nowadays because of the still too small volumes probed by galaxy surveys, might help constraining better its overall shape and break the degeneracy just described.

The addition of H_0 and supernovae measurements breaks the bias-shape degeneracy, returning parameters perfectly consistent with the Λ CDM cosmology. As for the previous section, the biggest change in precision is due to the SN, which improves the accuracy of the three parameters previously discussed, by a factor 2-3. The final constraints, when all four probes are used, are shown in Figures 14 and 15 by the green shaded areas enclosed within dot-dashed lines. For the quantities shown in the plot we obtain $\Omega_k = (4.5 \pm 6.5) \times 10^{-3}$ (36% increase in the errors with respect to Λ CDM case), $w_{DE} = -0.981^{+0.083}_{-0.084}$ (29% increase in the errors with respect to the w CDM case) and $\Omega_{DE} = 0.733^{+0.016}_{-0.017}$ (8% increase with respect to both).

6.5 Time varying dark energy equation of state parameter

In section 6.3 we encode possible deviations from the cosmological constant model in a constant effective dark energy equation of state. In this section we include explicitly a time dependency on w_{DE} through the simple parameterization of equation (9). We treat the two parameters of this model, w_0

**Figure 16.** Two-dimensional marginalised constraints of the w CDM parameter space in the $w_0 - w_a$ plane. Colour and line coding is the same as in Figure 9. The vertical and horizontal dotted lines show the values of these parameters for the flat Λ CDM case ($w_0 = -1$ and $w_a = 0$). The dotted diagonal line shows the equation $w_{DE}(a_p) = -0.97 = w_0 + (1 - a_p)w_a$, where $a_p = 0.65$ is the pivot scale factor from the combination of CMB and $P_{LRG}(k)$ (see text).

and w_a as free and we consider the curvature to be fixed 0. The constraints on the cosmological parameters for the cosmology analysed in this section from the different combinations of probes are listed in Table 9.

Figure 16 shows the two-dimensional marginalised constraints in the $w_0 - w_a$ plane from CMB alone (blue shaded

Table 9. Marginalised constraints on the cosmological parameters of the Λ CDM parameter space from the combination of probes listed in the header of the table. The quoted values are the same as in Table 3.

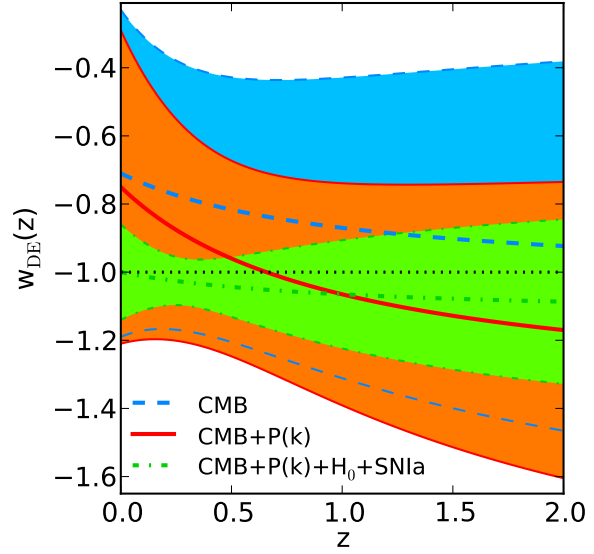
	CMB	CMB+ $P(k)$	CMB+ $P(k)$ + H_0	CMB+ $P(k)$ +SNIa	CMB+ $P(k)$ + H_0 +SNIa
$100\omega_b$	$2.249^{+0.052}_{-0.053}$	$2.253^{+0.050}_{-0.049}$	$2.255^{+0.049}_{-0.049}$	$2.251^{+0.050}_{-0.050}$	$2.257^{+0.049}_{-0.048}$
$100\omega_{DM}$	$10.99^{+0.52}_{-0.52}$	$11.27^{+0.43}_{-0.43}$	$11.31^{+0.43}_{-0.43}$	$11.30^{+0.43}_{-0.44}$	$11.29^{+0.45}_{-0.45}$
100Θ	$1.0399^{+0.0022}_{-0.0022}$	$1.0402^{+0.0022}_{-0.0022}$	$1.0402^{+0.0021}_{-0.0021}$	$1.0401^{+0.0022}_{-0.0022}$	$1.0403^{+0.0021}_{-0.0021}$
τ	$0.088^{+0.015}_{-0.015}$	$0.086^{+0.014}_{-0.014}$	$0.086^{+0.014}_{-0.014}$	$0.086^{+0.015}_{-0.015}$	$0.086^{+0.014}_{-0.014}$
w_0	$-0.71^{+0.47}_{-0.49}$	$-0.75^{+0.44}_{-0.48}$	$-1.04^{+0.31}_{-0.31}$	$-0.98^{+0.14}_{-0.14}$	$-1.00^{+0.14}_{-0.14}$
w_a	$-0.32^{+1.00}_{-1.01}$	$-0.63^{+1.07}_{-0.99}$	$-0.11^{+0.85}_{-0.86}$	$-0.15^{+0.52}_{-0.52}$	$-0.13^{+0.53}_{-0.53}$
n_s	$0.961^{+0.014}_{-0.013}$	$0.961^{+0.012}_{-0.012}$	$0.962^{+0.012}_{-0.012}$	$0.960^{+0.012}_{-0.012}$	$0.962^{+0.012}_{-0.012}$
$\log(10^{10} A_s)$	$3.065^{+0.033}_{-0.033}$	$3.074^{+0.031}_{-0.032}$	$3.075^{+0.032}_{-0.033}$	$3.074^{+0.032}_{-0.033}$	$3.075^{+0.032}_{-0.032}$
Ω_{DE}	$0.665^{+0.102}_{-0.102}$	$0.702^{+0.055}_{-0.054}$	$0.741^{+0.027}_{-0.028}$	$0.728^{+0.018}_{-0.018}$	$0.734^{+0.016}_{-0.016}$
Age [Gyr]	$13.921^{+0.295}_{-0.295}$	$13.741^{+0.118}_{-0.115}$	$13.699^{+0.102}_{-0.104}$	$13.733^{+0.109}_{-0.105}$	$13.710^{+0.104}_{-0.104}$
Ω_M	$0.335^{+0.102}_{-0.102}$	$0.298^{+0.054}_{-0.055}$	$0.259^{+0.028}_{-0.027}$	$0.272^{+0.018}_{-0.018}$	$0.266^{+0.016}_{-0.016}$
σ_8	$0.742^{+0.082}_{-0.080}$	$0.770^{+0.108}_{-0.104}$	$0.837^{+0.077}_{-0.076}$	$0.810^{+0.043}_{-0.044}$	$0.818^{+0.045}_{-0.045}$
z_{re}	$10.5^{+1.2}_{-1.2}$	$10.4^{+1.2}_{-1.2}$	$10.4^{+1.2}_{-1.2}$	$10.4^{+1.2}_{-1.2}$	$10.4^{+1.1}_{-1.1}$
H_0 [km s $^{-1}$ Mpc $^{-1}$]	$65.0^{+9.9}_{-9.7}$	$68.2^{+6.4}_{-6.2}$	$72.6^{+3.7}_{-3.7}$	$70.6^{+2.0}_{-2.0}$	$71.4^{+1.7}_{-1.7}$

areas within dashed lines), CMB plus LRG power spectrum (red shaded areas within solid lines) and the combination of CMB, $P_{LRG}(k)$, H_0 and SNIa (green shaded areas within dot-dashed lines). The vertical and horizontal dotted lines at $w_0 = -1$ and $w_a = 0$ show the values of the two parameters for the Λ CDM case. In the three cases a degeneracy is visible, which is reduced as more independent data are included. From CMB alone we obtain $w_0 = -0.71^{+0.47}_{-0.49}$ and $w_a = -0.32^{+1.00}_{-1.01}$; the inclusion of the LRGs power spectrum information does not change substantially the one-dimensional constraints ($w_0 = -0.75^{+0.44}_{-0.48}$ and $w_a = -0.63^{+1.07}_{-0.99}$) but reduces by almost a factor 2 the figure of merit, i.e. the area of the 95% confidence level (Albrecht et al. 2006). As shown in the previous two sections, supernovae have an important role in constraining dark energy properties and the inclusion of their information reduces the errors in the two parameters by about a factor 3 and 2, respectively. The one-dimensional constraints from the combination of all the datasets are $w_0 = -1.00 \pm 0.14$ and $w_a = -0.13 \pm 0.53$. The attempt to constrain also the time evolution of the dark energy equation of state results in a degradation of its present value.

From these results it is possible to reconstruct the time dependence of the dark energy equation of state parameter. The thick dashed, solid and dot-dashed lines in Figure 17 show the value of $w_{DE}(z)$ from CMB, CMB plus $P_{LRG}(k)$ and the combination of the four probes, respectively. The corresponding $1-\sigma$ errors, which vary with redshift, are indicated by the shaded areas within the thin lines. They are computed according to Albrecht et al. (2006):

$$\langle \delta w_{DE}^2(a) \rangle = \langle (\delta w_0 + (1-a)\delta w_a)^2 \rangle. \quad (16)$$

In the redshift range shown in the plot, w_{DE} is always compatible with a cosmological constant at the 1σ level. Furthermore the errors show a minimum at a redshift called “pivot” (Huterer & Turner 2001; Hu & Jain

**Figure 17.** $w_{DE}(z)$ as function of the redshift z as obtained from the constraints shown in Figure 16. The thick dashed blue, solid red and green dot-dashed lines are the mean $w_{DE}(z)$ for CMB, CMB+ $P_{LRG}(k)$ and CMB+ $P_{LRG}(k)$ + H_0 +SNIa. The blue, red and green dashed lines enclosed within the outermost dashed, solid and dot-dashed lines are the 68% confidence level for the same three combinations as computed from equation (16).

2004; Albrecht et al. 2006). For the three cases shown in Figure 17, we obtain a pivot redshift of $z_p = 0.4$ (CMB), $z_p = 0.54$ (CMB+ $P_{LRG}(k)$) and $z_p = 0.3$ (CMB+ $P_{LRG}(k)$ + H_0 +SNIa) and an equation of state parameter $w_{DE}(z_p) = -0.80 \pm 0.37$, $w_{DE}(z_p) = -0.97 \pm 0.29$ and $w_{DE}(z_p) = -1.03 \pm 0.069$. It is interesting to note that in the last case the precision is comparable to the one pre-

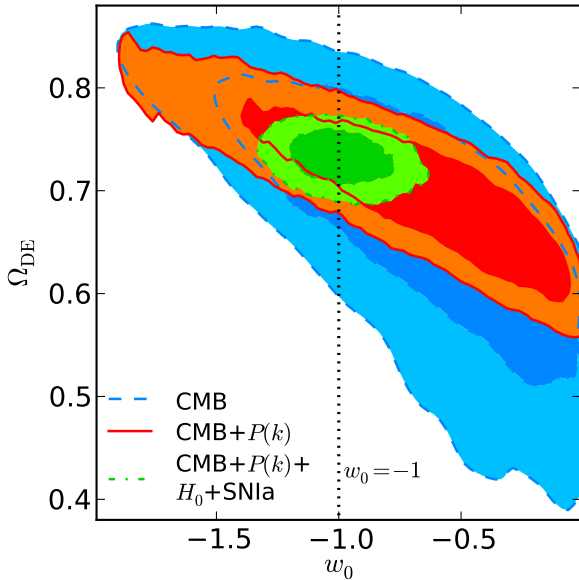


Figure 18. Two-dimensional marginalised constraints of the w CDM parameter space in the $w_0 - \Omega_{DE}$ plane. Colour and line coding is the same as in Figure 9. The vertical line is for $w_0 = -1$.

sented in Section 6.3. The diagonal dotted line in Figure 16 shows that the degeneracy between w_0 and w_a is very close to $w_0 + (1 - a_p)w_a = -0.97$, where $a_p = 0.65$ is the pivot scale factor from the $CMB + P_{LRG}(k)$ constraints.

Figure 18 shows the two-dimensional marginalised constraints in the $w_0 - \Omega_{DE}$ plane. The colour and line code is the same as in Figure 16. This figure illustrates that the addition of large scale structure information to the CMB data halves the errors on the dark energy density from $\Omega_{DE} = 0.66 \pm 0.10$ to $\Omega_{DE} = 0.702^{+0.055}_{-0.054}$. The inclusion of SNIa and H_0 measurements decreases the errors further by 70% to $\Omega_{DE} = 0.734 \pm 0.016$.

7 COMPARISON WITH PREVIOUS STUDIES

In this section we compare our results with recent work focused on the analysis of the large scale structure of the Universe. In Section 7.1 we perform a quantitative comparison of our results with those of Reid et al. (2010, thereafter R10), whose measurement and model are publicly available⁷. Section 7.2, instead, lists a number of similar analyses, for which this is not the case, and we can only discuss the differences qualitatively.

7.1 Reid et al. (2010)

The LRG distribution from the SDSS DR7 has already been used to extract cosmological parameters by R10. The analysis in that work differs from the one we perform mostly in five important details: i) all the LRGs from the Northern Galactic Cap and the 3 southern stripes were used (110576 galaxies in 7931 deg^2), ii) thanks to the count-in-cylinders

technique (CiC, Reid & Spergel 2009; Reid et al. 2009), the authors extracted a halo catalogue from the LRG distribution and then computed the halo power spectrum using the PVP estimator, iii) they computed the covariance matrix from 10000 lognormal catalogues (LN, Coles & Jones 1991), iv) they used a model based on HALOFIT (Smith et al. 2003), that required additional calibration against numerical simulations and v) they analysed the power spectrum in the range $0.02 h \text{ Mpc}^{-1} < k < 0.2 h \text{ Mpc}^{-1}$. The advantage of using the reconstructed underlying density field, instead of the galaxies, is that the intra-halo peculiar motions, which cause the so called fingers-of-gods, are erased, leaving weaker small scale redshift-space distortions. They combine their halo power spectrum with the 5th year data from the WMAP satellite (WMAP5, Komatsu et al. 2009) and the Union Supernovae dataset (Kowalski et al. 2008). The comparison between the results in table 3 of R10 and the corresponding ones in this work (third column in Tables 3, 5, 6 and third and fifth columns in Table 8) shows that, with the exception of the Λ CDM case and despite the smaller k modes used by us, the errors that we obtain here are slightly smaller and that there are significant offsets in the preferred values of some parameters. For example, the constraints on w_{DE} in the w CDM parameter space, when combining CMB and $P(k)$, are $w_{DE} = -1.02 \pm 0.13$ in our analysis and $w_{DE} = -0.79 \pm 0.15$ in R10.

As the full measurement from R10 and a COSMOMC module which includes the model is publicly available, we can understand the origin of the differences between the two studies. We concentrate here on the w CDM parameter space. Table 10 compares the results shown in the third column of Table 6 (second column) with the constraints that we obtain applying i) R10 model to our measurement (third column), ii) our model to R10 measurement (fourth column) and iii) R10 model to R10 measurement (last two columns). To do it, we combine the large scale structure information with the CMB measurements presented in Section 4.1, we consider the scales $0.02 h \text{ Mpc}^{-1} \leq k_i \leq 0.15 h \text{ Mpc}^{-1}$ and we compute the model for $k_j \leq 0.2 h \text{ Mpc}^{-1}$ before the convolution with the window function. In the last column we use $0.02 h \text{ Mpc}^{-1} \leq k_i \leq 0.20 h \text{ Mpc}^{-1}$ and $k_j \leq 0.50 h \text{ Mpc}^{-1}$, as originally done in R10. The similarity between the constraints obtained in this last case and those of R10 shows that the effect of using WMAP7 plus small angular scale CMB data instead of WMAP5 is very small. If we consider the parameters constrained mainly by the CMB (ω_b , ω_{DM} , Θ , τ , A_s , z_{re} and n_s) we find that they are, as expected, mostly independent of the power spectrum measurement and model used in the analysis. Excluding the last column, for the other parameters we find i) that, given a measurement, the errors that are obtained using the model of equation (3) are generally smaller than the ones from R10's model and ii) that, given a model, the parameters obtained from our measurement agree better with the bulk of the literature than the ones recovered from the R10 power spectrum. In particular, these data prefer larger values of w_{DE} and of Ω_M , which lead to smaller values of σ_8 and H_0 . Using $P_{LRG}(k)$ presented in Section 3.1 we measure the dark energy equation of state parameter to be $w_{DE} = -1.022^{+0.129}_{-0.128}$ when using our model and $-1.056^{+0.184}_{-0.191}$ when using R10 model. This is more than a 50% increase in the uncertainty.

⁷ <http://lambda.gsfc.nasa.gov/toolbox/lrgdr/>

Table 10. Comparison between this work and R10: marginalised constraints on the cosmological parameters of the Λ CDM parameter space from the combination of CMB and $P(k)$. The central four columns are for $0.02 h \text{ Mpc}^{-1} \leq k_i \leq 0.15 h \text{ Mpc}^{-1}$ and $k_j \leq 0.2 h \text{ Mpc}^{-1}$ while the last one for $0.02 h \text{ Mpc}^{-1} \leq k_i \leq 0.20 h \text{ Mpc}^{-1}$ and $k_j \leq 0.5 h \text{ Mpc}^{-1}$. The quoted values are the same as in Table 3.

	this work	$P_{\text{LRG}}(k)$ vs. R10 model	$P_{\text{R10}}(k)$ vs. our model	$P_{\text{R10}}(k)$ vs. R10 model	$P_{\text{R10}}(k)$ vs. R10 model, extended
$100\omega_b$	$2.251^{+0.049}_{-0.050}$	$2.251^{+0.049}_{-0.049}$	$2.246^{+0.050}_{-0.053}$	$2.257^{+0.055}_{-0.053}$	$2.259^{+0.053}_{-0.053}$
$100\omega_{\text{DM}}$	$11.25^{+0.43}_{-0.43}$	$11.92^{+0.43}_{-0.42}$	$11.04^{+0.46}_{-0.46}$	$11.22^{+0.50}_{-0.51}$	$11.18^{+0.46}_{-0.48}$
100Θ	$1.0402^{+0.0022}_{-0.0022}$	$1.0401^{+0.0021}_{-0.0021}$	$1.0399^{+0.0021}_{-0.0021}$	$1.0398^{+0.0022}_{-0.0022}$	$1.0399^{+0.0022}_{-0.0022}$
τ	$0.086^{+0.015}_{-0.015}$	$0.085^{+0.015}_{-0.015}$	$0.087^{+0.015}_{-0.015}$	$0.087^{+0.014}_{-0.015}$	$0.086^{+0.014}_{-0.014}$
w_{DE}	$-1.022^{+0.129}_{-0.128}$	$-1.056^{+0.184}_{-0.191}$	$-0.798^{+0.127}_{-0.127}$	$-0.847^{+0.172}_{-0.169}$	$-0.817^{+0.154}_{-0.152}$
n_s	$0.962^{+0.012}_{-0.012}$	$0.963^{+0.013}_{-0.013}$	$0.959^{+0.013}_{-0.012}$	$0.966^{+0.014}_{-0.014}$	$0.966^{+0.014}_{-0.014}$
$\log[10^{10} A_s]$	$3.073^{+0.034}_{-0.033}$	$3.102^{+0.032}_{-0.032}$	$3.066^{+0.034}_{-0.034}$	$3.078^{+0.032}_{-0.032}$	$3.075^{+0.030}_{-0.030}$
Ω_{DE}	$0.732^{+0.028}_{-0.028}$	$0.704^{+0.033}_{-0.032}$	$0.673^{+0.041}_{-0.041}$	$0.679^{+0.042}_{-0.041}$	$0.673^{+0.037}_{-0.036}$
Age [Gyr]	$13.733^{+0.118}_{-0.117}$	$13.755^{+0.118}_{-0.115}$	$13.932^{+0.148}_{-0.156}$	$13.889^{+0.154}_{-0.156}$	$13.905^{+0.141}_{-0.137}$
Ω_{M}	$0.268^{+0.028}_{-0.028}$	$0.296^{+0.032}_{-0.033}$	$0.327^{+0.041}_{-0.041}$	$0.321^{+0.041}_{-0.042}$	$0.327^{+0.036}_{-0.037}$
σ_8	$0.818^{+0.065}_{-0.064}$	$0.857^{+0.072}_{-0.069}$	$0.725^{+0.057}_{-0.057}$	$0.758^{+0.072}_{-0.071}$	$0.745^{+0.065}_{-0.066}$
z_{re}	$10.4^{+1.2}_{-1.2}$	$10.4^{+1.2}_{-1.2}$	$10.5^{+1.2}_{-1.2}$	$10.5^{+1.2}_{-1.2}$	$10.4^{+1.2}_{-1.1}$
$H_0 [\text{km s}^{-1} \text{ Mpc}^{-1}]$	$71.2^{+3.8}_{-3.8}$	$69.6^{+4.5}_{-4.3}$	$64.2^{+4.0}_{-3.9}$	$65.2^{+4.6}_{-4.7}$	$64.4^{+4.0}_{-4.1}$

If we consider the R10 measurement, we obtain, for the two models, $w_{\text{DE}} = -0.798^{+0.127}_{-0.127}$ and $-0.847^{+0.172}_{-0.169}$, with $w_{\text{DE}} > -1$ at 1.5 and 0.9 σ level, respectively. Including scales up to $0.2 h \text{ Mpc}^{-1}$, we measure $w_{\text{DE}} = -0.817^{+0.154}_{-0.152}$: the error decreases, but remains larger than when using our model, and disfavors the cosmological constant scenario at 1.2σ . These results clearly point towards differences in both the modelling and the measurement of the power spectrum.

While equation (3) makes use of only three free parameters and does not require any calibration, the model in R10 relies largely on numerical simulations in order to fix some of the parameters and to correct for the imprecision of HALOFIT, which at $k \approx 0.1 - 0.2 h \text{ Mpc}^{-1}$ can describe a Λ CDM power spectrum with about a 5% accuracy (see e.g. Heitmann et al. 2010). Furthermore the calibration is performed only against simulations that reproduce the clustering of a flat Λ CDM universe, which could potentially introduce biases for more general parameter spaces, as the comparison between the second and third column in Table 10 might suggest. The parameters shown in Tables 6-9 are almost insensitive to the cosmological model assumed, whilst the ones listed in table 3 of R10 exhibit larger variations. This might indicate that our model is better suited to analyse a large variety of cosmological parameter spaces.

The tension between the constraints obtained when using different measurements, instead, points in the direction of differences in the shape of the power spectrum or of the window matrix. Figure 19 shows the LRG power spectrum described in Section 3.1 (with blue points) and the halo one from R10 (red diamonds). The error-bars show the corresponding variances. Besides a factor of about four in the amplitude, due to the different samples and estimators used, which we include in the figure, the shapes of the two power spectra are almost identical, as we expect. We would also expect the window functions to be similar, but Figure 20 shows

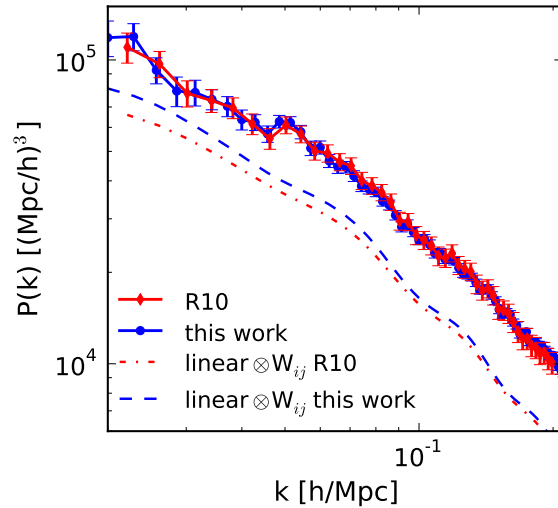


Figure 19. Comparison of the LRG power spectrum described in Section 3.1 (blue points) and the halo one from R10 (red diamonds) with the corresponding errors. The amplitude of the power spectrum from R10 has been increased by a factor 4 in order to make the comparison easier. The best fit linear power spectrum of Figure 2 convolved with the window matrix presented in Section 3.1 and from R10 are shown with a blue dashed and a red dot-dashed lines, respectively. In order to make the plot more readable, the amplitude of these two power spectra is not matched to the one of P_{LRG} .

that the rows of $W(k_i, k_j)$ corresponding to the k -bands of the measured power spectra are substantially different. This is intriguing, given that the bulk of our and R10 samples the same. This difference is even clearer when convolving a model $P(k)$ with the window function. The dashed and dot-

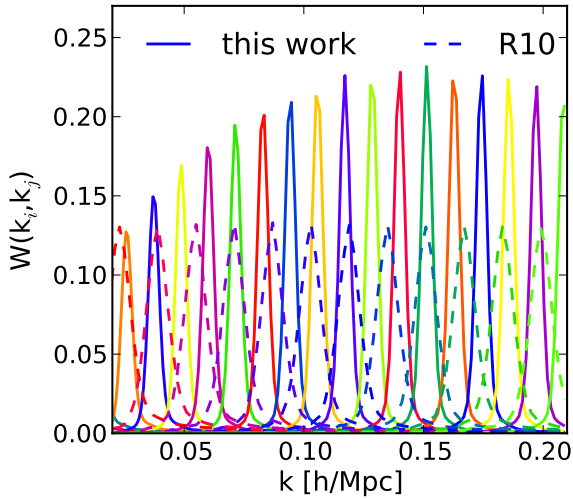


Figure 20. Comparison of the rows of the window matrix corresponding to the k -bands of the measured LRG power spectrum analysed in this work (solid lines) and from R10 (dashed lines). For clarity only one every fourth row is shown.

dashed lines in Figure 19 show the best fit linear power spectrum from Figure 2 after the convolution with our and R10 $W(k_i, k_j)$, respectively. In order to avoid clutter the amplitude of these two power spectra is not matched to $P_{\text{LRG}}(k)$. The differences in the window matrix are transformed into different shapes of the convolved $P_{\text{lin}}(k)$, which implies that these measurements cannot be described by the same set of cosmological parameters. This difference in the window matrix is responsible for the main differences shown in Table 10.

7.2 Other works

Percival et al. (2010) analysed almost 900,000 galaxies from the combination of the full SDSS DR7 galaxy sample and the two-degree Field Galaxy Redshift Survey (2dFGRS, Colless et al. 2003) and extracted the BAO feature from the power spectrum in 7 redshift bins. The main cosmological results are shown in their table 5 and can be compared with the third column in Tables 3, 5 and 6 and with Table 8. Their constraints are compatible with ours and with the findings of R10. Significantly, despite the much smaller sample that we use, the constraints that we obtain are comparable or tighter than the ones of Percival et al. (2010). As an example, for the Λ CDM case we obtain from CMB+ $P_{\text{LRG}}(k)$ $w_{\text{DE}} = -1.02 \pm 0.13$, while they report the value $w_{\text{DE}} = -0.97 \pm 0.17$, which corresponds to an improvement of about 25% in our results. This comparison suggests the importance of the use of the full information content in the galaxy power spectrum, as already noticed by different authors (e.g., Sánchez, Baugh & Angulo 2008; Shoji, Jeong & Komatsu 2009; Blake et al. 2011).

The correlation function has also been intensively used with similar goals. Sánchez et al. (2009) applied a model equivalent to the one presented in section 5.1 (Crocce & Scoccimarro 2008; Sánchez, Baugh & Angulo 2008) to the correlation function of the LRG sample from the

SDSS DR6, as measured by Cabré & Gaztañaga (2009a). Combining this with Union SNIa sample and the CMB measurements from WMAP5, as well as with the position of the BAO peak along the line of sight in the two-dimensional correlation function from Gaztañaga, Cabré & Hui (2009), they extracted cosmological parameters for the same parameter spaces presented in this work. The overall results of Sánchez et al. (2009) are consistent with the ones presented in section 6. Interestingly our errors on the cosmological parameters are systematically smaller when curvature is kept as free variable and larger for the w CDM and Λ CDM cases. This shows that the models and the measurements of the power spectrum and the correlation function, although generally coherent, show some small differences in the sensitivity to cosmological parameters for different parameter spaces. In the Λ CDM case, the constraints of Sánchez et al. (2009) show the same bias-shape degeneracy that shifts the values of Ω_k and w_{DE} upwards with respect to the flat Λ CDM paradigm (compare Figure 14 with figure 14 in Sánchez et al. (2009)). The inclusion of SNIa and of H_0 (radial BAO) in our (their) analysis leads to the tightest constraints in both works. For flat and non flat Λ CDM, the differences are negligible, while for the other three cases, where SNIa measurements play an important role, the errors that we obtain are larger: this is due to the inclusion of the supernovae systematic errors, which were neglected in Sánchez et al. (2009), in our analysis. When we do not use the systematics, we obtain tighter constraints, shown by the middle column of Table 7. In this case we measure the dark energy equation of state parameter to be $w_{\text{DE}} = -1.007 \pm 0.046$, about 11% tighter than the corresponding value measured by Sánchez et al. (2009, $w_{\text{DE}} = -0.969 \pm 0.052$).

A more recent analysis of the correlation function from the DR7 LRG sample has been made by Chuang, Wang & Hemantha (2010), using a simplified version of the model presented by Reid et al. (2010). They combined this measurement with WMAP7 and Union2 data in order to extract cosmological parameters. Some of their constraints are offset by $1-2\sigma$ with respect to our findings and their measurements of the dark energy equation of state are compatible with ours, once the SNIa systematics are neglected. Carnero et al. (2011) measured the angular correlation function and detected the BAO feature from the LRGs in the SDSS DR7 photometric catalogue, which consists of a sample of about 1.5 million galaxies. Fixing all the other parameters, with the exception of H_0 , to the best fit from WMAP7, they measure w_{DE} to be -1.03 ± 0.16 .

The small scale clustering has also been used to perform cosmological analyses. From the small scale projected correlation function and mass-number ratio in clusters, modelled in the halo model framework, Tinker et al. (2011) extracted cosmological and model parameters, obtaining, when combining with WMAP7, $\Omega_M = 0.290 \pm 0.016$ and $\sigma_8 = 0.826 \pm 0.02$. The difference between these results and the values of Table 3 might be due to the smaller number of cosmological degrees of freedom and the higher number of model parameters.

In a recent article Blake et al. (2011) presented the first cosmological results from the WiggleZ survey (Drinkwater et al. 2010). They used a sample of about 130,000 emission line galaxies across 1000 deg^2 in the red-

shift range $0.3 < z < 0.9$. From the correlation function, the power spectrum, the BAOs and the band-filtered correlation function (Xu et al. 2010) they extracted BAO parameters, like the effective distance $D_V(z)$ of equation (15) and the “acoustic parameter”, defined by $A(z) \equiv D_V \sqrt{\Omega_M H_0^2} / cz$ (Eisenstein et al. 2005). From those, they measured cosmological parameters for the Λ CMD and the w CDM models. When using LSS information only, the uncertainties are large but the results show a strong preference for the presence of dark energy, with $w_{DE} = -1.6^{+0.6}_{-0.7}$. Combining the BAO parameters with WMAP7 distance priors they measured the dark energy equation of state parameter to be $w_{DE} = -0.982^{+0.154}_{-0.189}$, which became $w_{DE} = -1.026 \pm 0.081$ if also Union2 SN are used. Those results are in agreement with ours, although their uncertainties are about 20-30% larger than the ones that we show in Table 6. The agreement between our results and the ones in Blake et al. (2011) show that, despite the differences in the galaxies selected, the survey volume and geometry and the procedure used to extract cosmological information, both analyses are robust enough for the precision achievable today.

8 SUMMARY AND CONCLUSIONS

We have computed the power spectrum of the distribution of about 90,000 luminous red galaxies, extracted from the spectroscopic part of the seventh data release of the Sloan Digital Sky survey. To compute the covariance matrix for the power spectrum we make use of the 160 LasDamas mock catalogues, which have the same angular and redshift distribution as the observed LRGs. We describe the measured power spectrum with a model inspired by renormalised perturbation theory and modified in order to describe biased objects in redshift space (section 5.1). This model has been successfully tested against numerical simulations (M10) and mock catalogues (section 5.4) for $k \lesssim 0.15 h \text{ Mpc}^{-1}$ at $z=0-0.5$.

Combining the large scale structure information with measurements of the CMB temperature and polarisation power spectrum from the seven year data release of WMAP, ACBAR, BOOMERanG, CBI and QUAD and with the luminosity-distance relation from the Union2 supernovae sample and using a precise determination of the local Hubble parameter as a gaussian prior, we explore the constraints in five different cosmological parameter spaces described in section 5.2. They are the flat Λ CDM concordance model, a similar one where curvature is a free parameter ($k\Lambda$ CDM) and three models in which the dark energy equation of state has a parametric form: in two cases it is assumed to be constant, with and without the assumption of a flat geometry (w CDM and kw CDM), and in the last case (wa CDM) we model w_{DE} with the simple parametric formula of equation (9).

Overall, we obtain tight constraints on the cosmological parameters for all the five cases and we do not detect deviations from the flat Λ CDM paradigm. The different combinations of the four experiments used in this analysis do not show any evidence of tensions between cosmological probes. We find that the curvature is null at $1-\sigma$ level with errors of the order of $10^{-2} - 10^{-3}$. We measure the dark energy equation of state parameter to be consistent with a cosmo-

logical constant with 13% uncertainty for $\text{CMB}+P_{\text{LRG}}(k)$ and 6.5% uncertainty for $\text{CMB}+P_{\text{LRG}}(k)+H_0+\text{SNIa}$ in the flat w CDM case. If we discard the systematic errors in the SNIa, the precision increases to 4.6%. In the kw CDM, because of the added degree of freedom, we have a degradation of the constraints to 8.4%, when combining all the four samples. The constraints obtained with the CMB and large scale structure together are shifted by $1.5-2\sigma$ with respect to the best fit Λ CDM because of a bias-shape degeneracy in the power spectrum that allows very large, and unphysical, values of the bias when w_{DE} , Ω_M , Ω_k increase and σ_8 decreases. If we assume the parametric form of equation (9) for the dark energy equation of state, we obtain $w_{DE}(z=0.54) = -0.97 \pm 0.29$ ($\text{CMB}+P_{\text{LRG}}(k)$) and $w_{DE}(z=0.3) = -1.03 \pm 0.069$ (all four experiments combined). The latter is only slightly worse than the flat w CDM result.

In the near future new and larger galaxy redshift catalogues both spectroscopic, like BOSS and HETDEX, and photometric, like Pan-STARRS and DES, will become available, together with the new measurements of the CMB anisotropies from the Planck satellite (Ade et al. 2011). These datasets will enable us to improve the constraints presented in this work even further. Some of these experiments are explicitly designed in order to extract the maximum amount of information regarding dark energy. This would allow to exclude many classes of dark energy models or of modifications of general relativity. In order to use the full information from the power of these new large scale observations and to avoid introducing systematic effects, accurate models of the large scale distribution, scale dependent bias and redshift space distortions are necessary. In M10 we showed that the model used in this work is accurate enough to describe the power spectrum shape also for surveys with volumes larger than available nowadays. The explicit inclusion of bias and redshift space distortions in the model would allow however to use a larger range of scales than now possible, helping to improve the quality of the cosmological constraints even further.

ACKNOWLEDGMENTS

We thank the LasDamas project for releasing publicly the mock catalogues. We thank Shaun Cole and Andrés Balaguera-Antolínez for discussions about the power spectrum computation and Friedrich Röpke and Sandra Benítez for the clarifications about SNIa. FM acknowledges support by the Trans-regional Collaborative Research Centre TRR33 The Dark Universe of the German Research Foundation (DFG).

Funding for the SDSS and SDSS-II has been provided by the Alfred P. Sloan Foundation, the Participating Institutions, the National Science Foundation, the U.S. Department of Energy, the National Aeronautics and Space Administration, the Japanese Monbukagakusho, the Max Planck Society, and the Higher Education Funding Council for England. The SDSS Web Site is <http://www.sdss.org/>.

The SDSS is managed by the Astrophysical Research Consortium for the Participating Institutions. The Participating Institutions are the American Museum of Natural History, Astrophysical Institute Potsdam, University of

Basel, University of Cambridge, Case Western Reserve University, University of Chicago, Drexel University, Fermilab, the Institute for Advanced Study, the Japan Participation Group, Johns Hopkins University, the Joint Institute for Nuclear Astrophysics, the Kavli Institute for Particle Astrophysics and Cosmology, the Korean Scientist Group, the Chinese Academy of Sciences (LAMOST), Los Alamos National Laboratory, the Max-Planck-Institute for Astronomy (MPIA), the Max-Planck-Institute for Astrophysics (MPA), New Mexico State University, Ohio State University, University of Pittsburgh, University of Portsmouth, Princeton University, the United States Naval Observatory, and the University of Washington.

REFERENCES

- Abazajian, K. N., et al., 2009, *ApJS*, 182, 543
 Abbott T. et al., 2005, preprint (arXiv:astro-ph/0510346)
 Ade P. A. R. et al., 2011, preprint (arXiv:1101.2022)
 Amanullah R. et al., 2010, *ApJ*, 716, 712
 Albrecht A. et al., 2006, preprint (arXiv:astro-ph/0609591)
 Angulo R., Baugh C. M., Frenk C. S., Lacey C. G., 2008, *MNRAS*, 383, 755
 Astier P. et al., 2006, *A&A*, 447, 31
 Balaguera-Antolínez A., Sánchez A. G., Böhringer H., Collins C., Guzzo L., Phleps S., 2011, *MNRAS*, in press
 Bengochea G. R., 2011, *PhLB*, 696, 5
 Berlind A. A., Weinberg D. H., 2002, *ApJ*, 575, 587
 Bernardeau F., Colombi S., Gaztañaga, E., Scoccimarro R., 2002, *PhR*, 367, 1
 Bernardeau F., Crocce M., Scoccimarro R., 2008, *PhRvD*, 78, 10352
 Blake C. et al., 2011, arXiv, arXiv:1105.2862
 Brown M. L. et al., 2009, *ApJ*, 705, 978
 Cabré A., Gaztañaga E., 2009, *MNRAS*, 393, 1183
 Cabré A., Gaztañaga E., 2009, *MNRAS*, 396, 1119
 Carnero A., Sanchez E., Crocce M., Cabre A., Gaztanaga E., 2011, preprint (arXiv:1104.5426)
 Chevallier M., Polarski D., 2001, *IJMPD*, 10, 213
 Chuang C.-H., Wang Y., Hemantha M. D. P., 2010, preprint (arXiv:1008.4822)
 Cole S. et al., 2005, *MNRAS*, 362, 505
 Coles P., Jones B., 1991, *MNRAS*, 248, 1
 Colless M. et al., 2003, preprint (arXiv:astro-ph/030658)
 Cooray A., Sheth R., 2002, *PhR*, 372, 1
 Christensen N., Meyer R., preprint (arXiv:astro-ph/0006401)
 Crocce M., Scoccimarro R., 2006, *Phys. Rev. D*, 73, 063519
 Crocce M., Scoccimarro R., 2006, *Phys. Rev. D*, 73, 063520
 Crocce M., Scoccimarro R., 2008, *Phys. Rev. D*, 77, 023533
 Davis M., Geller M. J., 1976, *ApJ*, 208, 13
 Davis M., Efstathiou G., Frenk C. S., White S. D. M., 1985, *ApJ*, 292, 371
 Drinkwater M. J. et al., 2010, *MNRAS*, 401, 1429
 Dunkley J. et al., 2009, *ApJS*, 180, 306
 Efstathiou G. et al., 2002, *MNRAS*, 330, L29
 Eisenstein D. J., Hu W., 1998, *ApJ*, 496, 605
 Eisenstein D. J., Hu W., 1998, *ApJ*, 511, 5
 Eisenstein D. J. et al., 2001, *AJ*, 122, 2267
 Eisenstein D. J. et al., 2005, *ApJ*, 633, 560
 Eisenstein D. J. et al., 2011, preprint (arXiv:1101.1529)
 Elia A., Kulkarni S., Porciani C., Pietroni M., Matarrese S., 2010, preprint (arXiv:1012.4833)
 Fang W., Hu W., Lewis A., 2008, *PhRvD*, 78, 087303
 Feldman H. A., Kaiser N., Peacock J. A., 1994, *ApJ*, 426, 23
 Frieman J. A. et al., 2008, *AJ*, 135, 338
 Frigo M., Johnson S. G., 2005, *Proceedings of the IEEE*, 93, 216
 Gaztañaga E., Cabré A., Hui L., 2009, *MNRAS*, 399, 1663
 Gelman A., Rubin D. B., 1992, *Stat. Sci.*, 7, 457
 Gilks W. R., Richardson S., Spiegelhalter, D. J., 1996, *MarkovChain Monte Carlo in Practice*. Chapman and Hall, London, UK
 Guy J. et al., 2007, *A&A*, 466, 11
 Heitmann K., White M., Wagner C., Habib S., Higdon D., 2010, *ApJ*, 715, 104
 Hicken M., Wood-Vasey W. M., Blondin S., Challis P., Jha S., Kelly P. L., Rest A., Kirshner R. P., 2009, *ApJ*, 700, 1097
 Hill G. J., Gebhardt K., Komatsu E. & MacQueen P. J., 2004, *The New Cosmology: Conference on Strings and Cosmology*, 743, 224
 Hinshaw G. et al., 2003, *ApJS*, 148, 135
 Holsclaw T., Alam U., Sansó B., Lee H., Heitmann K., Habib S., Higdon D., 2010, *PhRvD*, 82, 103502
 Hu W., Jain B., 2004, *PhRvD*, 70, 043009
 Huff E., Schulz A. E., White M., Schlegel D. J., Warren M. S., 2007, *APH*, 26, 351
 Huterer D., Starkman G., 2003, *PhRvL*, 90, 031301
 Huterer D., Turner M. S., 2001, *PhRvD*, 64, 123527
 Jarosik N. et al., 2010, preprint (arXiv:1001.4744)
 Jha S., Riess A. G., Kirshner R. P., 2007, *ApJ*, 659, 122
 Jennings E., Baugh C. M., Pascoli S., 2011, *MNRAS*, 410, 2081
 Jeong D., Komatsu E., 2006, *ApJ*, 651, 619
 Jeong D., Komatsu E., 2009, *ApJ*, 691, 569
 Jones W. C. et al., 2006, *ApJ*, 647, 823
 Kaiser N. et al., 2002, *SPIE*, 4836, 154
 Kazin E. A. et al., 2010, *ApJ*, 710, 1444
 Kessler R. et al., 2009, *ApJS*, 185, 32
 Komatsu E. et al., 2009, *ApJS*, 180, 330
 Komatsu E. et al., 2011, *ApJS*, 192, 18
 Kowalski M. et al., 2008, *ApJ*, 686, 749
 Kuo C. L. et al., 2007, *ApJ*, 664, 687
 Larson D. et al., 2011, *ApJS*, 192, 16
 Laureijs R., 2009, preprint (arXiv:0912.0914)
 Lewis A., Bridle A., 2002, *Phys. Rev. D*, 66, 103511
 Lewis A., Challinor A., Lasenby A., 2000, *ApJ*, 538, 473
 Linder E. V., 2003, *PhRvL*, 90, 091301
 McDonald P., *Phys. Rev. D*, 2006, 74, 103512
 McDonald P., *Phys. Rev. D*, 2007, 75, 043514
 MacTavish C. J. et al., 2006, *ApJ*, 647, 799
 Masjedi M. et al., 2006, *ApJ*, 644, 54
 Matarrese S., Pietroni M., 2007, *JCAP*, 06, 26
 Matarrese S., Pietroni M., 2008, *Mod. Phys. Lett. A*, 23, 25
 Matsubara T., 2004, *ApJ*, 615, 573
 Matsubara T., 2008, *Phys. Rev. D*, 77, 063530
 Matsubara T., 2008, *Phys. Rev. D*, 78, 083519
 Montesano F., Sánchez A. G., Phleps S., 2010, *MNRAS*, 408, 2397
 Montroy T. E. et al., 2006, *ApJ*, 647, 813

Moresco M., Jimenez R., Cimatti A., Pozzetti L., 2010, preprint (arXiv:1010.0831)

Norberg P. et al., 2001, MNRAS, 328, 64

Norberg P. et al., 2002, MNRAS, 332, 827

Peebles P. J. E., Yu J. T., 1970, ApJ, 162, 815

Peebles P. J., Ratra B., 2003, Rev. Mod. Phys., 75, 559

Percival W. J. et al., 2002, MNRAS, 337, 1068

Percival W. J., Verde L., Peacock J. A., 2004, MNRAS, 347, 645

Percival W. J., Cole S., Eisenstein D. J., Nichol R. C., Peacock J. A., Pope A. C., Szalay A. S., 2007, MNRAS, 381, 1053

Percival W. J. et al., 2010, MNRAS, 401, 2148

Perlmutter S. et al., 1999, ApJ, 517, 565

Phleps S., Peacock J. A., Meisenheimer K., Wolf C., 2006, A&A, 457, 145

Piacentini F. et al., 2006, ApJ, 647, 833

Pietroni M., 2008, JCAP, 10, 36

Reichardt C. L. et al., 2009, ApJ, 694, 1200

Reid B. A., Spergel D. N., 2009, ApJ, 698, 143

Reid B. A., White M., 2011, preprint (arXiv:1105.4165)

Reid B. A., Spergel D. N., Bode P., 2009, ApJ, 702, 249f

Reid B. A. et al., 2010, MNRAS, 404, 60

Riess A. G. et al., 1998, AJ, 116, 1009

Riess A. G. et al., 2004, ApJ, 607, 665

Riess A. G. et al., 2007, ApJ, 659, 98

Riess A. G. et al., 2009, ApJ, 699, 539

Riess A. G., et al., 2011, ApJ, 730, 119

Samushia L., Percival W. J., Raccanelli A., 2011, preprint (arXiv:1102.1014)

Sánchez A. G., Cole S., 2008, MNRAS, 385, 830

Sánchez A. G., Baugh C. M., Percival W. J., Peacock J. A., Padilla N. D., Cole S., Frenk C. S., Norberg P., 2006, MNRAS, 366, 189

Sánchez A. G., Baugh C. M., Angulo, R., 2008, MNRAS, 390, 1470

Sánchez A. G., Crocce M., Cabre A., Baugh C. M., Gaztanaga E., 2009, MNRAS, 400, 1643

Schlegel D., White M., Eisenstein D., 2009, preprint (arXiv:0902.4680)

Scoccimarro R., 2004, Phys. Rev. D, 70, 083007

Serra P., Cooray A., Holz D. E., Melchiorri A., Pandolfi S., Sarkar D., 2009, Phys. Rev. D, 80, 121302

Shoji M., Jeong D., Komatsu E., 2009, ApJ, 693, 1404

Sievers J. L. et al., 2009, preprint (arXiv:0901.4540)

Smith R. E. et al., 2003, MNRAS, 341, 1311

Smith R. E., Scoccimarro R., Sheth R. K., 2008, PhRvD, 77, 043525

Smith R., Hernández-Monteagudo C., Seljak U., Phys. Rev. D, 2009, 80, 063528

Spergel D. N. et al., 2003, ApJS, 148, 175

Spergel D. N. et al., 2007, ApJS, 170, 377

Sugiyama N., 1995, ApJS, 100, 28

Sunyaev R. A., Zeldovich Y. B., 1970, Ap&SS, 7, 3

Taruya A., Hiramatsu T., 2008, ApJ, 674, 617

Taruya A., Nishimichi T., Saito S., Hiramatsu T., 2009, PhRvD, 80, 123503

Taruya A., Nishimichi T., Saito S., 2010, PhRvD, 82, 063522

Tegmark M., Silk J., Blanchard A., 1994, ApJ, 420, 484

Tegmark M. et al., 2004, ApJ 606, 702

Tinker J. L. et al., 2011, preprint (arXiv:1104.1635)

Tsujikawa S., 2010, LNP, 800, 99

Vikhlinin A. et al., 2009, ApJ, 692, 1060

Wood-Vasey W. M. et al., 2007, ApJ, 666, 694

Xu X. et al., 2010, ApJ, 718, 1224

Zehavi I. et al., 2002, ApJ, 571, 172

APPENDIX A: BASIC EQUATIONS TO COMPUTE THE POWER SPECTRUM

In this section we summarise the basic equations of the FKP and PVP estimators used to compute the power spectrum and the window function from galaxy surveys. PVP is a generalisation of FKP and takes in account the change of the galaxy bias with the luminosity of the galaxies (see e.g., Davis & Geller 1976; Norberg et al. 2001, 2002; Zehavi et al. 2002; Phleps et al. 2006).

The observed power spectrum $P_o(k)$ is obtained from the squared average Fourier transform of the weighted density field defined by

$$\text{FKP: } F(\mathbf{x}) = \frac{1}{N} w(\mathbf{x}) [n_g(\mathbf{x}) - \alpha n_r(\mathbf{x})], \quad (\text{A1a})$$

$$\text{PVP: } F(\mathbf{x}) = \frac{1}{N} \int dL \frac{w(\mathbf{x}, L)}{b(\mathbf{x}, L)} [n_g(\mathbf{x}, L) - \alpha n_r(\mathbf{x}, L)], \quad (\text{A1b})$$

where $n_g(\mathbf{x}, L)$ and $n_r(\mathbf{x}, L)$ are the number density of galaxies and randoms of luminosity L at position \mathbf{x} . The corresponding quantities of equation (A1a) can be obtained integrating over the luminosity. $w(\mathbf{x})$, $w(\mathbf{x}, L)$ are weighting functions and $b(\mathbf{x}, L)$, only PVP, is the bias relative to a specific galaxy population with luminosity L_* . The normalisation N is defined by

$$\text{FKP: } N^2 = \int d^3x \bar{n}^2(\mathbf{x}) w^2(\mathbf{x}), \quad (\text{A2a})$$

$$\text{PVP: } N^2 = \int d^3x \left[\int dL \bar{n}(\mathbf{x}, L) w(\mathbf{x}, L) \right]^2, \quad (\text{A2b})$$

where $\bar{n}(\mathbf{x}, L)$ and $\bar{n}(\mathbf{x})$ are, respectively, the mean expected number density, i.e. in absence of clustering, of galaxies of luminosity L at position \mathbf{x} and its integral over L . Finally α is a constant introduced to match the two catalogues and is chosen requiring that⁸ $\langle F(\mathbf{x}) \rangle = 0$:

$$\text{FKP: } \alpha = \frac{\int d^3x w(\mathbf{x}) n_g(\mathbf{x})}{\int d^3x w(\mathbf{x}) n_r(\mathbf{x})}, \quad (\text{A3a})$$

$$\text{PVP: } \alpha = \frac{\int d^3x dL [w(\mathbf{x}, L)/b(\mathbf{x}, L)] n_g(\mathbf{x}, L)}{\int d^3x dL [w(\mathbf{x}, L)/b(\mathbf{x}, L)] n_r(\mathbf{x}, L)}. \quad (\text{A3b})$$

The observed power spectrum can be then written for both estimators as:

$$P_o(\mathbf{k}) = \int \frac{dk'^3}{(2\pi)^3} P_t(\mathbf{k}') G^2(\mathbf{k} - \mathbf{k}') = \langle |F(\mathbf{k})|^2 \rangle - P_{\text{sn}}, \quad (\text{A4})$$

where $P_t(\mathbf{k}')$ is the “true” underlying power spectrum, the shot noise P_{sn} is given by

$$\text{FKP: } P_{\text{sn}} = \frac{1 + \alpha}{N^2} \int d^3x \bar{n}(\mathbf{x}) w^2(\mathbf{x}), \quad (\text{A5a})$$

⁸ In FKP, the authors use a definition of α such that $N = 1$.

$$\text{PVP: } P_{\text{sn}} = \frac{1+\alpha}{N^2} \int d^3x dL \bar{n}(\mathbf{x}, L) \frac{w^2(\mathbf{x}, L)}{b^2(\mathbf{x}, L)} \quad (\text{A5b})$$

and $G^2(k)$ is the window function, which encodes information about the survey geometry.

It can be shown that the window function is computed from the spherical averaged Fourier transform of the field

$$\text{FKP: } \bar{G}(\mathbf{x}) = \frac{1}{N} \bar{n}(\mathbf{x}) w(\mathbf{x}), \quad (\text{A6a})$$

$$\text{PVP: } \bar{G}(\mathbf{x}) = \frac{1}{N} \int dL \bar{n}(\mathbf{x}, L) w(\mathbf{x}, L), \quad (\text{A6b})$$

as $G^2(k) = \langle |\bar{G}(k)|^2 \rangle - G_{\text{sn}}$. G_{sn} is the shot noise defined by

$$\text{FKP: } G_{\text{sn}} = \frac{1}{N^2} \int d^3x \bar{n}(\mathbf{x}) w^2(\mathbf{x}), \quad (\text{A7a})$$

$$\text{PVP: } G_{\text{sn}} = \frac{1}{N^2} \int d^3x dL \bar{n}(\mathbf{x}, L) w^2(\mathbf{x}, L). \quad (\text{A7b})$$

In this work, we use the weighting functions, designed to minimise the variance, proposed in FKP and Cole et al. (2005):

$$\text{FKP: } w(\mathbf{x}) = \frac{w_i}{1 + P(k)n(\mathbf{x})} \quad (\text{A8a})$$

$$\text{PVP: } w(\mathbf{x}, L) = \frac{w_i b^2(\mathbf{x}, L)}{1 + P(k) \int dL b^2(\mathbf{x}, L) n(\mathbf{x}, L)}. \quad (\text{A8b})$$

The intrinsic weight of the objects, w_i , can contain information about completeness and/or fibre collision (Zehavi et al. 2002; Masjedi 2006). $P(k)$ is an estimate of the recovered power spectrum and it is usually substituted with a constant p_w , chosen in order to minimise the variance around the wave-number \bar{k} for which $P(\bar{k}) \sim p_w$.

APPENDIX B: IMPACT OF WEIGHTS ON POWER SPECTRA AND COSMOLOGICAL CONSTRAINTS

In the following we test the impact of p_w , w_i and estimator on the LRG and mock power spectra, on the errors and on the cosmological parameters.

B1 Testing the luminous red galaxies power spectrum

In this appendix we test the impact of different choices of the estimator, p_w and w_i on the LRG power spectrum and window function. For both estimators, FKP and PVP, we test four values of $p_w = 40000, 10000, 4000, 0$. We also consider four different intrinsic weights: i) $w_i = 1$ (all the objects have equal weight), ii) $w_i = c$ (areas with low completeness have less weight than areas with higher one), iii) $w_i = fc$ (the loss of galaxies due to fibre collisions is compensated as described in Section 3.1) and iv) $w_i = c \times fc$ (both completeness and fibre collision corrections applied).

Figure B1 shows the differences in the power spectra measured with the FKP (upper panel) and PVP (lower panel) estimators for the different choices of p_w and w_i . For clarity, in the figure we show only the combination of

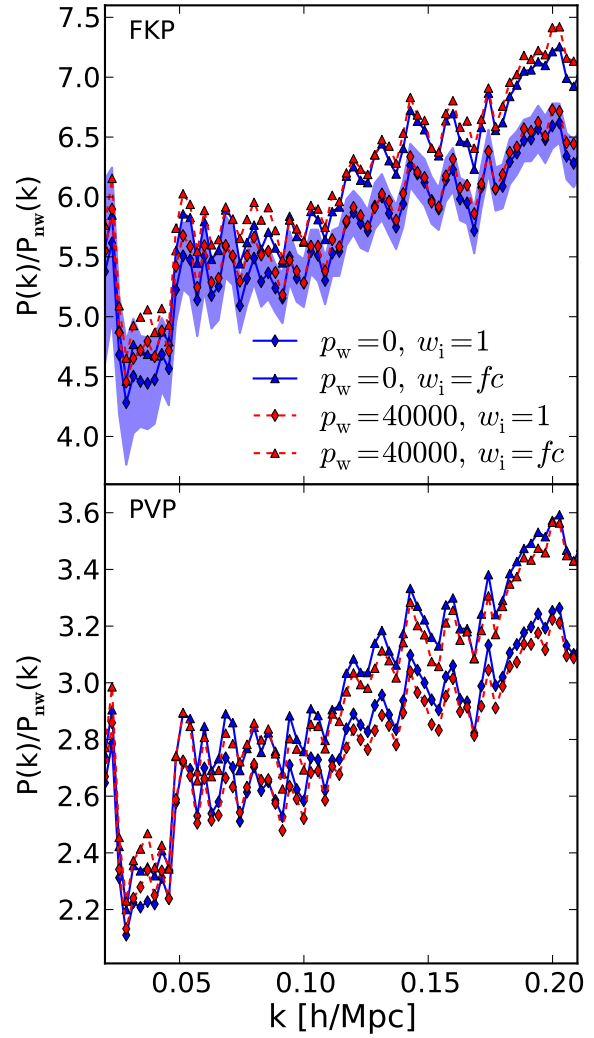


Figure B1. Comparison between power spectra computed with $p_w = 40000, 0$ (red dashed and blue solid lines) and $w_i = 1, fc$ (diamonds and up triangles) divided by a linear power spectrum without BAOs. The upper panel is for the FKP, the lower for PVP. The shaded area denotes the standard deviation computed from the mock catalogues using $p_w = 40000$.

$p_w = 40000, 0$ (red dashed and blue solid lines respectively) and $w_i = 1, fc$ (diamonds and up triangles, respectively). The shaded area shows the standard deviation as measured from the mock catalogues for $p_w = 40000$. All the power spectra have been divided by a non-wiggle one with the same cosmological parameters as the mock catalogues. Different choices of p_w change marginally the shape of the power spectrum. The results for $p_w = 10000, 4000$ fall in between the two extreme cases shown in Figure B1.

Instead, the correction for fibre collision has a significant effect. When obtaining spectra of crowded fields, not all the objects of interest can be targeted with a limited number of pointings. Because of this loss of objects, the amplitude of the highest peak in the density fields decreases, while the low density regions are unaffected. This causes the amplitude of the fluctuations, and consequently of the power spectrum, to be lower. We have indeed measured a few percent scale

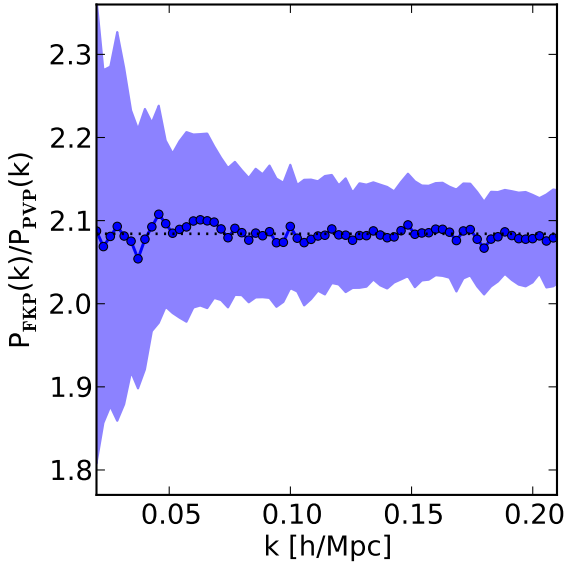


Figure B2. Ratio between power spectra computed the FKP and PVP estimators for $p_w = 40000$, $w_i = f_c$. The shaded area shows the standard deviation computed from the mock catalogues for $p_w = 40000$. The dotted horizontal line is the mean of the ratio in the plotted interval. The other choices of p_w and w_i show similar behaviour.

independent decrease in the amplitude of $\langle |F(\mathbf{k})|^2 \rangle$ (i.e. the power spectrum before subtracting the shot noise) in the case when fibre collision correction is not applied. This difference is visible at the large scale, low k , limit in Figure B1 where the power spectrum with the fibre collision (triangles) is always larger than the one without (diamonds). On the other side the shot noise (equations A5) depends on the expected non-clustered number density (\bar{n}) and the associated weights, which are not influenced (or influenced in a uniform way) by fibre collisions. This causes the shot noise to be the same in both cases, changing the shape of the final power spectrum $P_o(k)$. This effect is clearly visible in the small scale, large k , limit in Figure B1, where the fibre collision corrected power spectra become increasingly larger than the non corrected ones. We do not show the results when completeness correction is included, since the measured power spectra overlap almost exactly the non corrected ones. This is because both the galaxy and the random catalogues are weighted in the same way, therefore the density fluctuation field $F(\mathbf{k})$ is unchanged.

Comparing the two panels of Figure B1, it is clear that the choice of the estimator has a strong impact on the recovered power spectra: in the PVP case the amplitude is systematically lower than for FKP. Figure B2 shows the ratio of the power spectrum computed with the latter estimator with respect to the one computed with the former for the case $p_w = 40000$, $w_i = f_c$. As before, the shaded area corresponds to the standard deviation computed from the LasDamas catalogues. Although the amplitude is different, the relative bias between the two estimators is scale invariant in the range $0.02 h \text{ Mpc}^{-1} \leq k \leq 0.2 h \text{ Mpc}^{-1}$. This is expected from the fact that the galaxy sample that we use is almost volume limited and contains a very uniform population of galaxies.

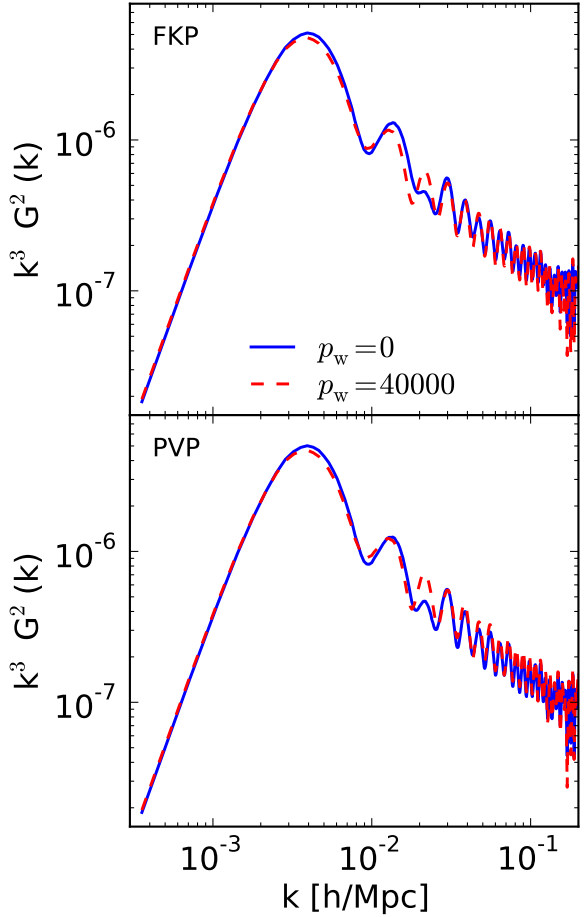


Figure B3. Window functions $G^2(k)$ multiplied by the cube of the wave-number k as function of k for $p_w = 0, 40000$ (solid and dashed lines, respectively) for $w_i = 1$. The upper panel is for FKP, the lower for PVP.

Recently, Balaguera-Antolínez et al. (2010) have shown that, in volume limited mock catalogues of the REFLEX II cluster survey, the power spectrum computed with the PVP estimator has higher correlations than the FKP one already at $k > 0.15 h \text{ Mpc}^{-1}$. Because of this and of the scale independent relative bias, we can safely use the power spectra as estimated with FKP in order to constrain cosmological parameters.

The window function, describing only the radial and angular selection function of the survey, is not affected by fibre collision effect; on the other hand different choices of p_w and the completeness correction change the weights of equations (A8), which influence the effective survey volume. As for the power spectrum, we do not measure differences when the completeness weighting is applied. Figure B3 shows the “dimensionless” window function $k^3 G^2(k)$ computed with FKP (upper panel) and PVP (lower panel) for $p_w = 40000, 0$ (dashed and solid line respectively). Although the overall shape is similar, there are small differences in the oscillations due to different effective volumes in the two cases. The results for $p_w = 10000, 4000$ fall in between the two extreme cases. The difference between the FKP and PVP window functions are negligible.

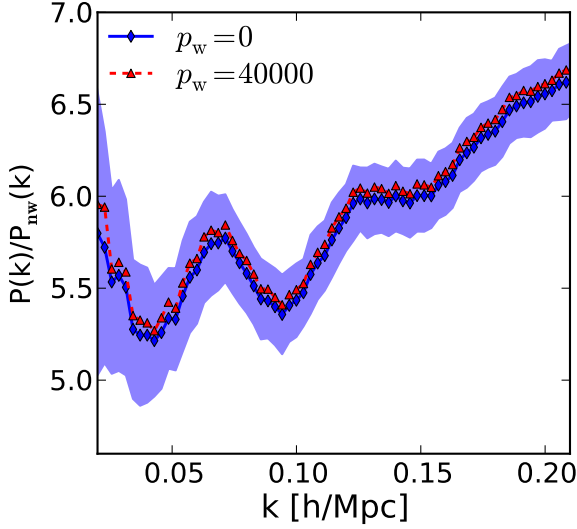


Figure B4. Comparison between mean mock power spectra computed for $p_w = 40000, 0$ (red dashed with triangles and blue solid lines with diamonds respectively) divided by a power spectrum without oscillations. The shaded area denotes the standard deviation for $p_w = 40000$.

When convolving these window functions with a linear power spectrum as in equation (1), the differences in the range $0.02 \, h \, \text{Mpc}^{-1} \leq k \leq 0.2 \, h \, \text{Mpc}^{-1}$ are negligible.

B2 Testing the power spectra of the mock catalogues

In order to test the impact of p_w on the results from the LasDamas, we compute the power spectra of the 160 mocks, their mean, standard deviation and covariance matrix for $p_w = 40000, 10000, 4000, 0$. Figure B4 shows the mean power spectra computed for the two extreme cases: the only difference is a small change in amplitude, which confirms the findings of the previous appendix, i.e. that the impact of different p_w on the computed power spectrum is negligible. The shaded area denotes the standard deviation for $p_w = 40000$.

The choice of p_w has, however, a large effect on the errors. Figures B5 and B6 show, respectively, the correlation matrix for $p_w = 40000$ (upper panel) and $p_w = 0$ (lower panel) and their difference. At $k \sim 0.1 \, h \, \text{Mpc}^{-1}$, for $p_w = 40000$ we measure that the correlation is systematically, although not significantly, lower than for $p_w = 0$. This is expected since, when using FKP, $P(k \sim 0.1) \simeq 40000$. At larger wave-number the power spectrum amplitude is smaller than at $k \sim 0.1 \, h \, \text{Mpc}^{-1}$ and the variance and the correlation are smaller for small values of p_w . This justifies our choice of using $p_w = 40000$ in our analysis, since the amplitude of the power spectrum is of this order in the range of scales we are interested in. If the analysis were centred on the small scale power spectrum or correlation function, a smaller value of p_w would be preferable.

B3 Impact on the cosmological parameters

Here we test how the differences in the shape of the LRG power spectrum and the covariance matrix influence the cos-

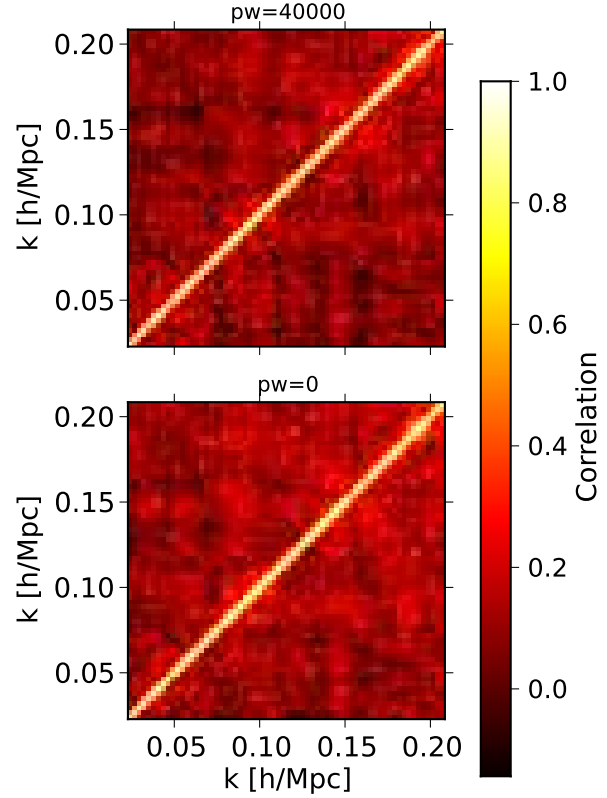


Figure B5. Correlation matrices for $p_w = 40000, 0$ (upper and lower panels respectively).

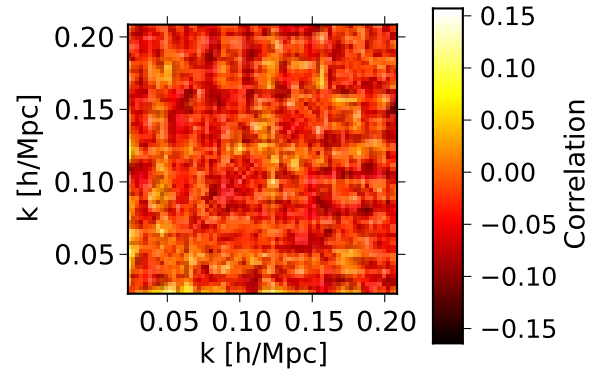


Figure B6. Differences between the $p_w = 40000$ and the $p_w = 0$ correlation matrices.

mological parameters measured assuming the Λ CDM cosmology. We combine the LSS information with the WMAP7 data.

Contrary to our expectations based on the results shown in Appendix B1, the cosmological parameters are much more sensible to p_w than to w_i . For a fixed p_w the covariance matrix is the same and only the shape of the power spectrum changes. As the shape of the power spectrum is not affected by the completeness correction, also the cosmological constraints are insensitive to it. The fibre collision correction

instead changes the bias, over which we marginalise analytically, without affecting the shot noise amplitude. Differences in the relative amplitude of the latter term can be absorbed at least partially by the mode coupling amplitude A_{MC} , which is systematically, although not significantly, larger when the loss of galaxies due to fibre collisions is corrected for. Because of this, cosmological constraints remain almost unchanged for different w_i . Changes of p_w instead influence the covariance but only marginally the power spectrum. The differences in the former influence the cosmological parameters, which differ by $0.5 - 1\sigma$, for $p_w = 40000$ and 0. For example I obtain the dark energy equation of state parameter to be $w_{DE} = -1.02 \pm 0.13$ for $p_w = 40000$ and $w_{DE} = -1.10 \pm 0.14$ for $p_w = 0$.

Given the precision that is possible to achieve with the data used in this article, the differences just highlighted are not distinguishable from the uncertainties in the parameters. But in future, given the big improvements expected, these effects might become important and will need further analysis.

This paper has been typeset from a \LaTeX file prepared by the author.